Fine–scale structure in cometary dust tails I: analysis of striae in comet C/2006 P1 (McNaught) through temporal mapping

Icarus 319 (2019) 540–557

Contents lists available at ScienceDirect

Icarus

journal homepage: www.elsevier.com/locate/icarus

Fine-scale structure in cometary dust tails I: Analysis of striae in Comet C/2006 P1 (McNaught) through temporal mapping

Oliver Price[*,a,b], Geraint H. Jones[a,b], Jeff Morrill[c,1], Mathew Owens[d], Karl Battams[c], Huw Morgan[e], Miloslav Drückmuller[f], Sebastian Deiries[g]

[a] Mullard Space Science Laboratory, Department of Space and Climate Physics University College London, Holmbury St. Mary, Dorking, Surrey RH5 6NT, UK
[b] The Centre for Planetary Sciences at UCL/Birkbeck, London, UK
[c] Naval Research Laboratory, Washington, DC, USA
[d] Space and Atmospheric Electricity Group, Department of Meteorology, University of Reading, UK
[e] Aberystwyth University, Aberystwyth, Wales, UK
[f] Institute of Mathematics, Faculty of Mechanical Engineering, Brno University of Technology, Czech Republic
[g] European Organisation for Astronomical Research in the Southern Hemisphere, Garching bei München, Germany

ARTICLE INFO

Keywords:
Comets
Dust
Plasma
Solar wind

ABSTRACT

Striated features, or *striae*, form in cometary dust tails due to an as-yet unconstrained process or processes. For the first time we directly display the formation of striae, at C/2006 P1 McNaught, using data from the SOHO LASCO C3 coronagraph. The nature of this formation suggests both fragmentation and shadowing effects are important in the formation process. Using the SOHO data with STEREO-A and B data from the HI-1 and HI-2 instruments, we display the evolution of these striae for two weeks, with a temporal resolution of two hours or better. This includes a period of morphological change on 2007 January 13–14 that we attribute to Lorentz forces caused by the comet's dust tail crossing the heliospheric current sheet. The nature of this interaction also implies a mixing of different sized dust along the striae, implying that fragmentation must be continuous or cascading. To enable this analysis, we have developed a new technique – temporal mapping – that displays cometary dust tails directly in the *radiation beta* (ratio of radiation pressure to gravity) and dust *ejection time* phase space. This allows for the combination of various data sets and the removal of transient motion and scaling effects.

1. Introduction

When active, comets release dust grains of various sizes and morphologies (e.g. Schulz et al., 2015; Hilchenbach et al., 2016). The grains' trajectories are influenced by solar radiation pressure to form dust tails, which lag behind the nucleus's motion about its orbit, e.g. Fulle (2004). Analysis of dust tails' structure can reveal key information on the dust grains' parameters, together with the time of release from the nucleus. These parameters can in turn provide information on the activity of the nucleus.

Features commonly observed in cometary dust (type II) tails include *synchronic bands*, which are large-scale linear features that are coaligned with the position of the comet's nucleus, and, much more rarely, *striae*. The latter are puzzling features that have only been observed in a few, generally very high production rate comets, including C/1957 P1 (Mrkos) (Sekanina, Z, Farrell, 1982), C/1962 C1 (Seki-Lines) (McClure, 1962), C/1975 V1 (West) (Koutchmy and Lamy, 1978; Lamy and Koutchmy, 1979; Nishioka et al., 1992), and C/1996 O1 (Hale-Bopp) (Sekenina and Pittichová, 1997).

Comet C/2006 P1 McNaught – for brevity, from hereon referred to as *McNaught* only – was discovered by Robert McNaught on 2006 August 7 (McNaught, 2006), and reached perihelion on 2007 January 12 at a distance of 0.17 AU from the Sun. This was well inside the perihelion distance of planet Mercury, and therefore a near-Sun comet (Jones et al., 2018). Undoubtedly a modern example of a "Great Comet", it was easily visible from Earth through much of January 2007, but only from the southern hemisphere when at its most spectacular post-perihelion. The orbit of McNaught suggests it is was a dynamically new comet from the Oort cloud (Marsden, 2007).

Combi et al. (2011) found that the comet's water production rate

* Corresponding author at: Mullard Space Science Laboratory, Department of Space & Climate Physics, University College London, Holmbury St. Mary, Dorking, Surrey RH5 6NT, UK.
E-mail address: oliver.price.15@ucl.ac.uk (O. Price).
[1] Now at: NASA Headquarters, Heliophysics Division, 300 E ST., SWWashington, DC 20546, USA

https://doi.org/10.1016/j.icarus.2018.09.013
Received 26 February 2018; Received in revised form 25 July 2018; Accepted 11 September 2018
Available online 12 September 2018

could be approximated by $5.4 \times 10^{29} r^{2.4}$ s^{-1}, where r is the heliocentric distance, and that it reached a peak of 5.48×10^{31} molec s^{-1} on 2007 January 13. Despite the comet's spectacular appearance around perihelion, relatively few works have been published on it based on visible wavelength observations, largely due to the difficultly in observing the object with ground-based facilities, though ground-based observations of sodium emission from the comet were possible with a solar telescope (Leblanc et al., 2008). The comet had an extensive, highly structured dust tail, displaying many striae. Observations of the comet at infrared wavelengths reveal that it had larger and more compact porous grains than many other objects (Kelley et al., 2010; Wooden et al., 2014).

Here we report on the analysis of the striae observed in McNaught, which arguably possessed the most spectacular dust tail of recent times, and certainly the one for which is available the most comprehensive collection of observations to date. We apply a new reprojection technique, which we refer to as *temporal mapping*, to images of McNaught's dust tail acquired from several sources, allowing us to track the behaviour of striae in the comet's tail throughout the comet's perihelion passage.

We present a sequence of images captured by the *Large Angle and Spectrometric Coronagraph* (*LASCO*) on the ESA/NASA *Solar and Heliospheric Observatory* (*SOHO*) spacecraft, that appears to record clearly for the first time the formation of several striae. Together with data from the *Heliospheric Imagers* (*HI*) that form part of the wider *Sun-Earth Connection Coronal and Heliospheric Investigation* (*SECCHI*) remote sensing package on the twin NASA *STEREO-A* and *B* spacecraft, we track the formation and evolving appearance of numerous striae. We propose that the progressive realignment of many of these striae is due to interactions between electrically charged dust grains and the heliospheric magnetic field.

1.1. Striae formation theories

Most striae models describe formation through the fragmentation of larger dust particles. In addition to gravity, cometary dust grains are certainly strongly influenced by radiation pressure. As these two primary forces act in opposition to each other, the effective force acting on them is equivalent to *reduced gravity*. This is parameterised by the dimensionless constant β_r, given as:

$$\beta_r = \frac{\text{Radiation Force}}{\text{Gravitation Force}} \quad (1)$$

The fragmentation of grains leads to the spreading of dust grains over time due to a difference in the β_r parameter between individual particles.

Sekanina and Farrell (1980) proposed that stria formation is a two-step process. They posited that the striae's parent dust grains are released from the nucleus all with similar values. After a delay, these grains break up within a short period of time. Their fragments have a range of β_r values, and radiation pressure separates the grains according to β_r, forming near-linear structures. Under this scenario, along a single stria, there is expected to be a monotonic increase in β_r with increasing heliocentric distance.

This model has been found to agree well with observations of striae (e.g. Pittichová et al., 1997). However, there is a serious issue with the Sekanina and Farrell two-step fragmentation scenario, in that it is difficult to explain why parent grains would all fragment after approximately the same time delay. They suggested rotational bursting generally due to uneven radiation pressure over grains' surfaces, but this has not been widely accepted. Hill and Mendis (1980) suggested that the fragmentation of grains could occur due to electrostatic charging, with the few keV and more electrons required for this process originating in the closed current system of the induced cometary magnetotail.

Nishioka and Watanabe (1990) and Nishioka (1998) proposed a different scenario for the formation of striae. Rather than a two-step process, an almost continuous cascade of fragmentation was proposed. This cascade continues beyond where grains become too small to observe. This process would result in fragments of all values co-existing along the length of each stria. Sekenina and Pittichová (1997) pointed out that a relaxed fragmentation time should lead to wedge shaped striae, which are not observed.

Other models have also been proposed. These include those of Froehlich and Notni (1988) and Notni and Thaenert (1988), who suggested stabilising effects due to optical thickness of dust clouds. Steckloff and Jacobson (2016) considered that each stria is the result of the destruction of macroscopic sized (10–100m) boulders by rotational stresses from sublimation pressures.

2. Data

Around perihelion, McNaught's proximity to the Sun in the sky made ground-based observations particularly challenging. However, instruments aboard the SOHO, STEREO-A, and STEREO-B spacecraft provided excellent imaging data, allowing the comet's coma and tail structures to be monitored through the perihelion passage. The activation of the *SECCHI* heliospheric imagers aboard the then–recently launched twin *STEREO* spacecraft came just in time to capture the dust tail as the comet reached perihelion, and this event was also captured by the *SOHO LASCO C3* coronagraph.

The comet was well observed from Earth from the southern hemisphere post-perihelion, with some of the older dust features also seen in the northern hemisphere during the same period, despite the nucleus being below the horizon from those locations. We note that this is similar to the circumstances of Comet de Chéseaux (C/1743 X1) with its extensive, structured dust tail (Kronk, 1999). For this project we use the *SECCHI HI-1* and *HI-2* datasets from both *STEREO* spacecraft, as well as *LASCO C3* Clear and Blue filter data and various ground-based images. Fig. 1 summarizes the images obtained from all sources. Further details of each data source are provided below.

2.1. Stereo A SECCHI HI

The twin NASA *STEREO* spacecraft follow separate orbits around the Sun, moving progressively ahead of and behind the position of the Earth (Howard et al., 2008). Each spacecraft has two Heliospheric Imagers, *HI-1* and *HI-2*. These consist of CCD cameras pointed off axis from the sun. *HI-1* points closest to the sun with a field of view of 20° and solar offset of 14° (Eyles et al., 2009). The effective primary bandpass of the instrument is ~ 630–730 nm, with additional, weaker coverage of the wavelengths ~ 300–450 and ~ 900–1000 nm (Bewsher et al., 2010). Images are obtained onboard measuring 2048 pixel square, but were downsampled to 1024 pixel square images for transmission during the period of interest. The pixel scale of transmitted images is70″ pixel^{-1}. This corresponded to a physical resolution of 43 000 km at McNaught's head at perihelion. As the dust tail extended from the nucleus towards STEREO-A, the physical resolution for the tail was higher, reaching ~ 33 000 km pixel^{-1}.

At the time of the McNaught observations, both HI-1 instruments were being commissioned, and McNaught was serendipitously in the field of view as their observations on both spacecraft began. A few 2048 pixel-wide images were downlinked during commissioning, but given the large scale of the striae, these do not prove particularly useful for this purpose compared to the 1024 pixel-wide images. The data from this instrument were inferred to imply the presence of a neutral iron tail at McNaught (Fulle et al., 2007).

Fig. 2 shows an example image of McNaught from STEREO-A HI-1. The fine structure of the dust tail is clear, but several artefacts also appear. The HI imagers are primarily designed to image sunlight Thomson scattered by tenuous solar wind and transient structures within it, such as coronal mass ejections. The instrument is not designed to deal during standard operations with objects that are as bright as

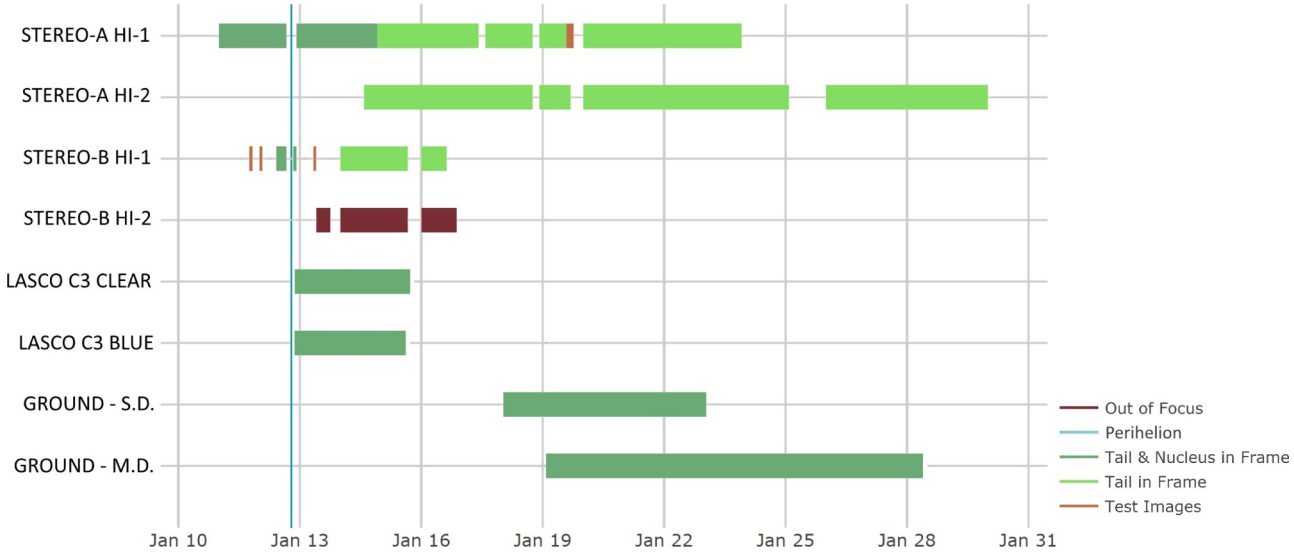

Fig. 1. Gantt chart summarising observations from all sources, including the different instruments aboard the STEREO-A, STEREO-B and SOHO spacecraft, and ground based images from authors S.D. and M.D.

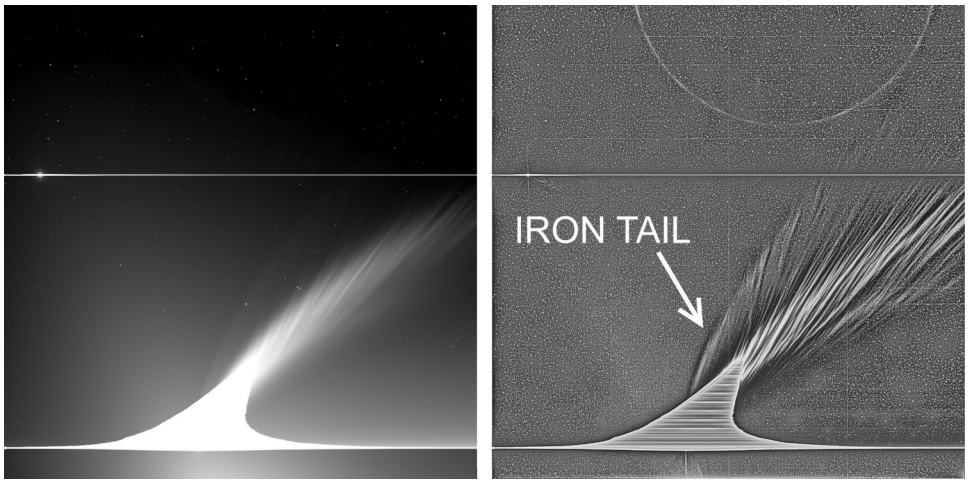

Fig. 2. (Left) The view of C/2006 P1 McNaught from STEREO-A HI-1 on 2007 January 14 at 00:01. The sun is centre below relative to both images (rotated 90° clockwise from nominal orientation). Apparent are several issues for the purpose of studying this comet, including the background intensity of the zodiacal dust at the bottom of the image, as well as overexposure and CCD bleeding around the nucleus and bright apparition of Venus (bright feature at upper left). (Right) The same image, enhanced with Multiscale Gaussian Normalisation. The process enhances fine-scale structure in the tail and the faint iron tail, as well as some artifacts, such as the semicircular feature at top, caused by an internal reflection in the instrument.

McNaught, hence much of the region around the coma is overexposed. The particularly bright coma of McNaught caused significant CCD bleeding. Furthermore, as the HI cameras do not have shutters (Eyles et al., 2009), as the pixel values are read off the detector, the camera continues to collect light, causing the bright background in parts of the image adjacent to the brightest tail regions.

The sequence of raw data from HI-1 can be viewed here:

With the Multiscale Gaussian Normalisation enhanced version (see Section 2.4.1 for details) viewable here:

The second of the two heliospheric imagers, HI-2, points further off axis with a field of view of 70° and solar offset of 53.7°, with the instrument designed to image CMEs all the way to the Earth (Eyles et al., 2009). The bandpass of HI-2 is centred on ~ 640 nm, with a FWHM of ~ 450 nm (Tappin et al., 2015). The pixel scale of transmitted HI-2 images is$4'$ pixel^{-1}, which corresponds to a physical scale at McNaught varying between 90 000 and 200 000km, depending on the position in the dust tail.

Although the nucleus of the comet did not pass into the HI-2 field of view, the extensive tail was present in the instrument data for approximately two weeks. Fig. 3 shows an example view of McNaught from STEREO-A HI-2. Here the fine structure of the tail is much dimmer than in HI-1 images. Complicating the interpretation of some of the images is the presence of zodiacal dust, whose surface brightness is comparable to that of the striae.

The sequence from HI-2 (difference image enhanced as per 2.4.2) can be viewed here:

2.2. STEREO B SECCHI HI

The HI instrument aboard STEREO-A has the same properties as its sister spacecraft, and both spacecraft were still very close to the Earth-Moon system at the time. The instrument door on STEREO-B opened for the first time on January 11, so the instrument was in a much earlier stage in its commissioning than its counterpart on STEREO-A. Many of its images contain artefacts, and there are fewer images taken at regular intervals. The default FITS headers for providing the celestial coordinates provided inconsistent results compared to the background starfields, so the astrometry for the files was recalculated independently using the automated service at *astrometry.net* (Lang et al., 2010).

We note in passing that true stereo images of Comet McNaught were taken by SECCHI HI-1A and HI-1B nineteen times between January 12 and 15. An example pair, from 00:01 on January 14, can be seen in Fig. 4. The parallax effect is clear in the two images, with a ~ 0.3° shift in background star positions. The separation of the two spacecraft was

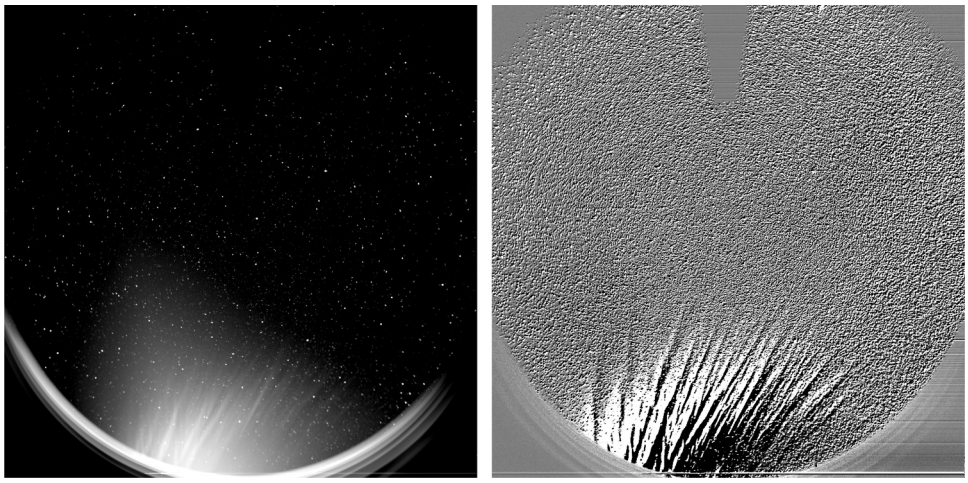

Fig. 3. (Left) The view of McNaught's dust tail from STEREO-A HI-2 on the 2007 January 19 at 00:01. The HI-1 frame and sun are below the image (rotated 90° clockwise from nominal orientation). The zodiacal dust is of comparable brightness to striae. (Right) A difference image of same frame. This image has been made by subtracting the preceding frame obtained 2 h earlier.

however too small to provide useful information on the three-dimensional distribution of the cometary dust to be extracted, e.g. to confirm that the dust lay exclusively in the comet's orbital plane. The HI-2 instrument aboard STEREO-B also captured the edge of the extended tail of McNaught. However, the instrument was unfortunately not in focus at this time and so this dataset was disregarded.

2.3. SOHO LASCO C3

The SOHO spacecraft resides ~ 1 million km sunward of Earth at Sun-Earth Lagrange Point L1. Its LASCO coronagraph images a 15° wide circle surrounding the Sun (Brueckner et al., 1995), and is responsible for the greatest number of comet discoveries (Battams and Knight, 2017). LASCO comprises three instruments; all the McNaught data were gathered using coronagraph C3, which covers 3.7 to 30 solar radii from the Sun's centre, recorded on 1024 by 1024 pixel images at a spatial resolution of 56 arcsec pix^{-1}. Further technical information on the LASCO instrument and its calibration is covered by Morrill et al. (2006).

Most McNaught images were gathered using a broadband "clear" filter covering wavelengths of 400 to 850 nm. These images, whilst capturing a great degree of detail in the dust tail, were overexposed in the comet's near-nucleus and coma regions. They suffer issues with overexposure of McNaught's bright nucleus, although the effect is less severe than with the STEREO heliospheric imagers. The instrument also includes 5 other narrower wavelength range filters (Morrill et al., 2006). As has also occurred with other anticipated bright comets, LASCO was commanded to obtain numerous images using the colour filters when McNaught was within the C3 field of view. In order to maximize data return, these images only included subframes of the entire C3 field of view, and were compressed onboard using a lossy algorithm prior to transmission to Earth. Despite the lower quality of these images compared to the clear images, they are very valuable for the study of the striae, as they record structures much closer to the comet's nucleus than in images obtained using the clear filter, which were generally overexposed around the comet's head. Although the clear filter images were least affected by data compression artifacts, much of the analysis of LASCO data here concentrates on images obtained using the instrument's blue filter.

The LASCO C3 Clear data was used with several calibration algorithms already applied, referred to as Level 1 calibration. These calibration steps include corrections for the flat field response of the detector, radiometric sensitivity, stray light, geometric distortion, and vignetting (Morrill et al., 2006). Unfortunately for the Blue filter dataset, Level 1 calibration is not available, and the raw level 0 data had to be used instead. In this analysis, as we concentrate on the morphology and dynamics of tail features and do not rely on any absolute calibration of the images, we deemed the unprocessed Level 0 images to be of sufficient quality for this study. This does however mean that the Sun's dust (F) corona and stray light are present in these images, but these largely structureless background features were largely removed by the enhancement techniques described below

Fig. 5 shows a LASCO clear filter image of the comet, enhanced with multiscale gaussian normalisation (Section 2.4.1). McNaught's nucleus was within the LASCO C3 field of view from 2007 January 12 01:42 UT to January 15 21:54 UT. The sunward edge of the dust tail remained in the field of view for several hours after the nucleus left, but with no clearly discernible structures visible within it.

The LASCO clear filter sequence (MGN enhanced as per Section 2.4.1) can be viewed here:

`Uploaded Media:soho_mgn_gif.gif`

Fig. 6 shows a combination of imaging data from SOHO LASCO and STEREO SECCHI HI-1 and HI-2, demonstrating the relative scales of the images returned by the different instruments.

2.4. Enhancement techniques

The dust tail striae are features present over a wide dynamic range in the images. Enhancement techniques were found to be required to trace the positions of the striae, and to also address the presence of zodiacal light in the images, i.e. the extension of the F corona. Two complementary enhancement techniques were employed. In presenting the enhanced images in this paper, as the brightness scale is largely arbitrary, we do not provide quantitative brightness values.

2.4.1. Multiscale Gaussian Normalisation

The large range in brightness over the tail region makes it difficult to extract fine structure information over the whole range of intensities and physical scales, even with the use of logarithmic brightness scaling. Morgan and Druckmüller (2014) developed the Multiscale Gaussian Normalisation technique, MGN, for application to such situations. At several length scales, convolution of the image with Gaussian kernels enables the calculation of local means and variance. These are used to offset and normalise pixel values locally to a mean of zero and unity standard deviation. The set of normalised images are then recombined into a global image, where fine structure across all parts of the image are visible. Fig. 2 shows the success of this method for revealing fine structure in cometary dust tails. The process is very efficient, working in a matter of seconds. We use this technique here for all three datasets.

2.4.2. Difference images

In certain cases MGN enhancement fails to enhance fine detail, probably due to noise. After the comet left the field of view of the *SECCHI* Heliospheric imagers, striae persisted in the tail and gradually faded from view. The features could eventually no longer be resolved by eye, even with MGN enhancement. However, difference images created by subtracting the previous image frame from each image reveal faint fine structure. This allows us to extend the useful range of data by several days.

2.5. Ground based data

The comet reached a peak magnitude of −5.5 (Marsden, 2007), when it was visible in the daylight sky near the Sun. Post-perihelion, it was easily visible to the naked eye in the southern hemisphere, when the nucleus was not observable from north of the equator. Some older striae were however visible from the northern hemisphere during that period. Many professional and amateur astronomers photographed the object. Here we have used wide angle photographs taken by author Sebastian Deiries at the European Southern Observatory in Chile, and wide angle photographs and composites taken by author Miroslav Drückmuller in Chile and Argentina.

3. Methodology

3.1. Motivation

Dust tail structures have traditionally been investigated using Monte-Carlo models of dust populations, and comparing the results directly to images of comets. Many such studies have been successful, but these approaches do have limitations. Kharchuk and Korsun (2010) reported on their efforts to model the striae visible in McNaught's tail. The results were somewhat satisfactory, but failed to reproduce the correct orientation of the striae, which in their simulations were aligned with the position of the comet's nucleus, and were therefore synchronic bands caused by variations in dust release rates at the nucleus.

Traditionally synchrone and syndyne lines are plotted alongside on overlaid onto images, which does allow for the model to be intuitively matched to the tail by eye. However, this method suffers due to the compression of lines near the nucleus, and rarefaction in the furthest and oldest regions of the tail. It is therefore difficult to relate dust features in these regions to one another, particularly across long time sequences where near nucleus features may have travelled out and reached the far tail, and especially when the viewing geometry or instrument has changed.

We introduce here a new dust tail analysis technique which presents dust features in a consistent way, by morphing images of comets onto a matrix of assumed dust age and sensitivity to solar radiation pressure. This temporal mapping technique has several advantages:

1. A single dust tail feature can be analysed over an extended period of time, despite changes in its physical scale, transient motion and viewing orientation
2. Changes in the dust tail during periods when the appearance of a tail changes rapidly can be easily resolved
3. Issues concerning observing geometry are removed, e.g. when the observer is close to the orbital plane of the comet and dust tail features are foreshortened
4. Images of an individual comet tail obtained by different observers can be easily compared
5. Important additional parameters, such as heliocentric distance, orbital plane coordinates and dust phase angle can be considered and evaluated for the observations

We have implemented the temporal mapping technique in Python, as detailed below. As McNaught was a very bright, high activity comet for which we have high quality dust tail imaging data, it is a perfect subject for the application of the technique.

3.2. The Finson Probstein model

The Finson–Probstein model provides a good basis for cometary dust tail modelling (Finson and Probstein, 1968). This assumes that only gravity and radiation pressure act on the dust grains after their release from the nucleus. Using the parameter β_r introduced in Section 1.1, an equation of motion for a dust particle can be based on the acceleration a, defined by:

$$a = \frac{-GM_s(1-\beta_r)}{r^2} \tag{2}$$

Where r is the heliocentric distance, a the acceleration of the dust outwards in the heliocentric radial direction, G the gravitational constant and M_s the solar mass. We make several assumptions in our use of the model:

1. The dust is ejected with zero velocity relative to the comet and hence the physics only evolves in two dimensions; the dust tail structure remains entirely in the orbital plane of the comet. Whilst the sublimating gas in reality imparts a velocity to the dust grains, the initial motion is smaller than the velocity imparted by radiation pressure and gravity. Studies of comets at orbital plane crossings show that the bulk of the dust tail remains close to the orbital plane to a reasonable approximation. However, there is some initial sorting of grain size due to smaller particles being accelerated to higher speeds before decoupling from the outflowing gas. As we assume the dust is sorted by the time it reaches the far tail, this is not significant.
2. The value of β_r is constant for a particular dust particle. As dust fragments or sublimates, the value of β_r will be affected. Striae models that include fragmentation and its effects are discussed in Section 1.1.
3. The optical thickness of the dust cloud does not affect the β_r value over time.

Note that our technique makes no assumptions about the mass or the physical cross-section of the individual dust grains. We only define a β_r value for each grain.

These assumptions reduce the problem to two parameters: β_r, and the time of dust particle emission, denoted by t_e. Each image is therefore deterministic, where every combination of β_r and t_e values maps to a unique position in the tail.

3.3. Creating a temporal map

Creating a temporal map requires the following:

1. Astrometry for the image; effectively right ascension, *RA*, and declination, *dec*, for every pixel. For spacecraft data in FITS format this is often accessible in the FITS metadata. For ground based images it can usually be determined using the *astrometry.net* website (Lang et al., 2010).
2. Orbital ephemerides for the comet and its observer location relative to the sun. We use ephemerides from NASA's JPL Horizons system (Giorgini et al., 1997). A one minute temporal resolution is used to guarantee positional accuracy.
3. The time of the image. For spacecraft data this is known, and many ground based observers provide this with their images. Otherwise it

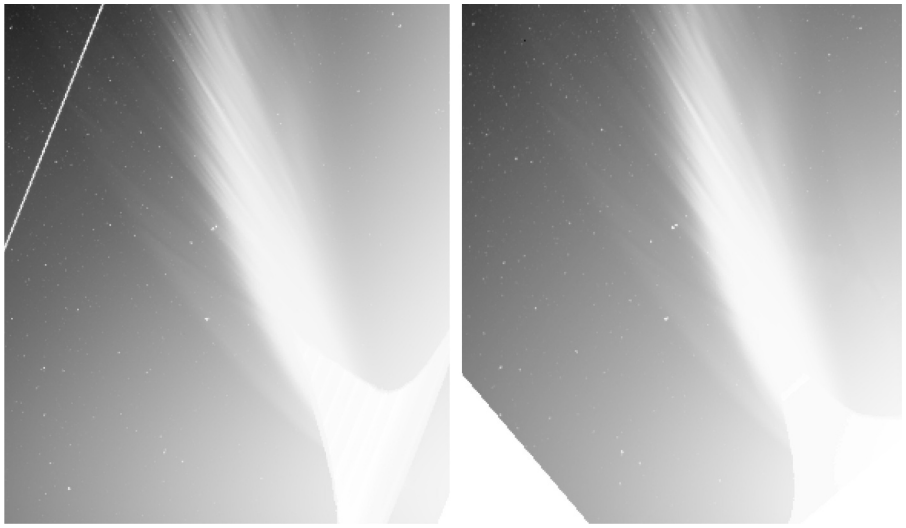

Fig. 4. A true stereo image pair of McNaught from STEREO-A (left) and STEREO-B (right) on 2007 January 14 at 00:01. The images have been rotated such that ecliptic north is upwards in both, and displayed with a histogram equalization-based brightness scaling.

is necessary to manually calculate this by using the celestial coordinates of the comet. If the astrometry for the background image is correct, then the exact position of the comet in the image and thus its location along its orbit can be used together with the orbit ephemeris to calculate the time at which an image was taken.

For a desired mapping with a known range of β_r and t_e, a temporal map is produced as follows:

1. Perform a trajectory simulation for each required β_r and t_e value. Using the t_e value, the corresponding initial condition of the comet is found. The dust is then numerically modelled using the following differential equations, which are adapted from Eq. (2):

$$\frac{d}{dt}\begin{pmatrix}\vec{r}\\ \vec{v}\end{pmatrix} = \begin{pmatrix}0 & 1\\ \frac{-GM_s(1-\beta_r)}{|\vec{r}|^3} & 0\end{pmatrix}\begin{pmatrix}\vec{r}\\ \vec{v}\end{pmatrix} \tag{3}$$

   To solve the numerical equation, we use the 4th order Runge Kutta method (Karim, 1966). The dust motion is calculated up until the light travel corrected time of the dust is exactly that at which the image was taken.
2. Once all the values are calculated and converted to *RA* and *dec*, the Finson-Probstein grid can be plotted over the image to give a visual check that the correct parameters have been used.
3. For each unique position in the image corresponding to particular values of β_r and t_e, a pixel value is extracted from the image. We convert the *RA* and *dec* coordinates of each modelled dust grain back into image coordinates using the FITS metadata, and linearly interpolate the four pixel values (from the four pixel centres that form the box containing the converted image coordinates) to get a pixel value for each β_r and t_e. We plot these pixel values with β_r on the new Y axis. The date and time of each t_e value is plotted on the X axis, for a selected range of dates.

For observations over several days, dust tail features can be held static in the temporal map, showing the evolution over time without relative motion effects from observer or comet. Furthermore, with multiple datasets, these maps can be mosaicked together. This allows not only for a comparative study of the same features observed with different instruments, but also for the dynamic range of the temporal map to be extended beyond the scope of single instruments.

3.4. Limitations

It is important to note that in producing the temporal maps, whilst the method does preserve the relative brightnesses of various parts of the tail, it does distort the relative apparent proportions of pixels with particular brightnesses. It is not therefore a tool for accurate photometric analysis, nor was it meant to be one.

In addition, we do not account for the strong phase angle dependencies encountered when observing forward scattered light, which contributes to the relative brightness gradient across the dust tail. Our method is not suitable for extracting dust size distributions, as we do not preserve the photometry nor consider the third dimensional aspect of the tail, e.g. Fulle (2004).

4. Results

4.1. Overview of McNaught tail features

From Earth and the cluster of spacecraft surrounding it, the orbit plane angle was $\sim 25^\circ$ at the start of observations on 2007 January 11, rising to a maximum of $\sim 35^\circ$ on January 16. This good viewing geometry, well outside the comet's orbital plane, allowed for the distinctive fan shape of the dust tail to be observed from Earth. At its most extensive, McNaught's tail reached visible lengths of just under 1 AU; on January 25, 15 day old dust of $\beta_r \sim 2$ extended to 0.975 AU from the nucleus.

The tail displayed a bimodal size distribution. Studying the dust maps with unprocessed data, the two peaks of this distribution appear centred on $\beta_r \sim 0.7$ and ~ 1.3.

The dust structures in the bimodal striated tail were generally visible for 12–16 days, although dust at lower β_r that was 24 days old could be discerned in difference images from STEREO-A HI-1. Using a combination of STEREO and ground based data (Fig. 7), a temporal map (Fig. 8) was produced showing three weeks' worth of dust being visible on 2007 January 21.

4.2. Striae morphology

Using the STEREO-A HI-1, HI-2 and the SOHO LASCO C3 Clear filter datasets, a sequence of 339 temporal maps was created, showing the main dust tail; i.e. $0.2 \leq \beta_r \leq 3$, from 2007 January 11 00:00 UT until

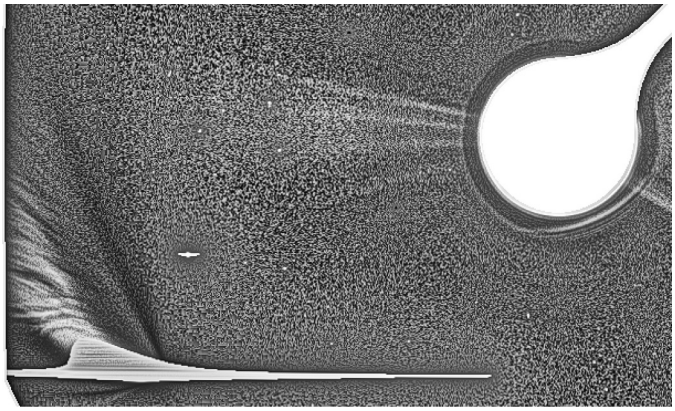

Fig. 5. The view of McNaught from the SOHO LASCO C3 coronagraph, using the clear filter, on January 15 at 00:53 UT. The image has been enhanced using the MGN technique (Section 2.4.1). The bright object near the comet is Mercury. Celestial north is up.

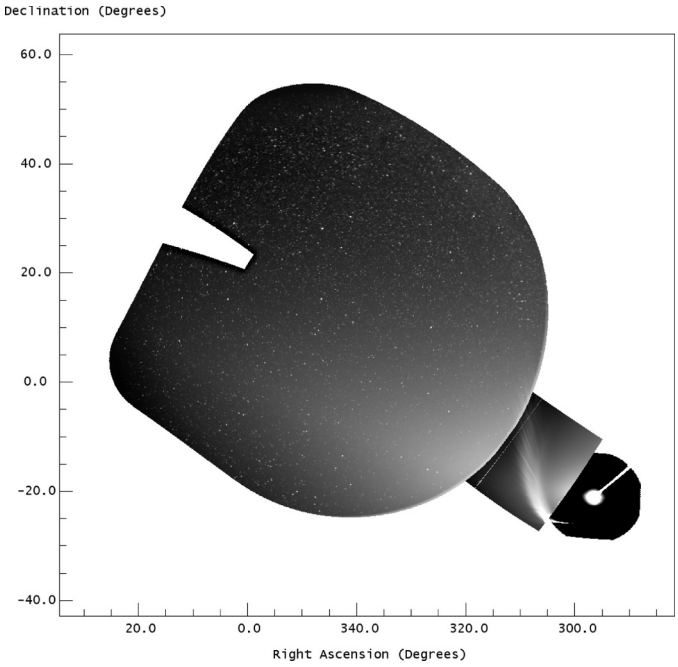

Fig. 6. The view of the comet as seen from STEREO and SOHO on 2007 January 15 at 12:00 UT. The SOHO LASCO C3 field of view is the region at lower right centred on the Sun. STEREO SECCHI HI1-A is the tilted square image containing the bulk of the comet's dust tail. The STEREO SECCHI HI2-A image is the leftmost panel, containing the outermost fringes of the dust tail, with the zodiacal light also apparent.

January 25 02:00 UT. This sequence is available as an animation at the following link:

Some selected frames from this sequence are shown in Fig. 9.

First, we note that all dust tail structures appear clearly and remain stationary with respect to both apparent nucleus release time and β_r in the temporal maps, which indicates the success of the method. Although striae generally appear linear in the original images, their profiles are curved in the projections presented here. The logarithmic β_r scale removes some of the curvature, allowing easier analysis of the features. If the striae had originated as nuclear outbursts, then they would appear as vertical features in the temporal maps, i.e. dust in each stria being of all the same apparent age. As expected based on earlier studies, striae instead appear inclined in these projections, implying that they do not form as near–instantaneous outbursts of dust of varying

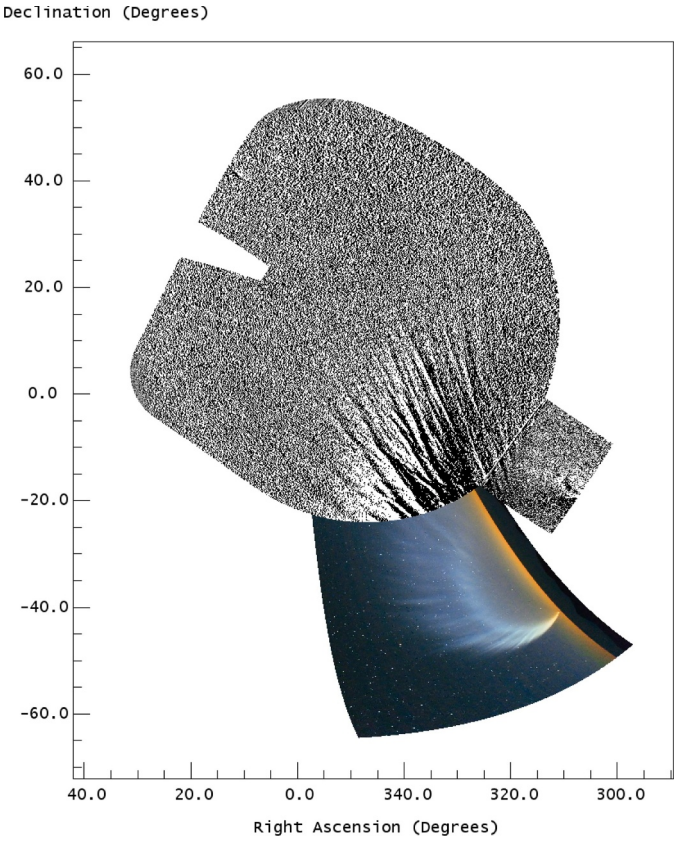

Fig. 7. The view of the comet as seen from STEREO and Earth on 2007 January 21 at 01:00 UT, in STEREO SECCHI HI1-A and HI2-A (both frames enhanced by subtraction of the preceding images to enhance differences), and a colour image taken from the European Southern Observatory, Chile by author SD.

β_r at the nucleus. The slope of the features implies that the highest β_r dust in each stria is youngest, and the lowest β_r particles the oldest. This interpretation is however dependent on a nucleus source.

The lowest β_r particles being the oldest sections of each stria is consistent with fragmentation of larger (generally lower β_r) grains leading to the release of lower mass (generally higher β_r) particles.

4.3. Neutral iron tail and associated features

Another noteworthy feature is the neutral iron tail. This appears as a separate, thin tail at high β_r. Theoretical calculations show that neutral iron would have an equivalent β_r of ~ 6, which provides a reasonable fit to the location of the tail (Fulle et al., 2007). Additionally, we note here from difference image from the HI-1 camera that material can be seen filling the gap between this iron tail and the main dust tail.

The iron tail was visible within both the STEREO-A HI-1 and HI-2 datasets. We created two maps to show this higher β_r region including features out to and including the iron tail. A series of 72 temporal maps using difference images shows features between $1 \leq \beta_r \leq 9$, from 00:00 UT on the 12th January 2007 until 00:00 UT on the 18th January. This sequence is available as an animation at the following link:

This sequence shows the material between the iron tail and main tail, and a frame from this sequence can be seen in Fig. 10.

Using the STEREO-A HI-1 data with a MGN enhancement, we created another series of 56 temporal maps focusing on the iron tail where $4 \leq \beta_r \leq 9$, from 2007 January 12 02:00 UT until January 16 20:00 UT. This sequence is available as an animation at the following link:

A frame from this sequence can be seen in Fig. 11.

The iron tail appears clearly, at high β_r. Our temporal mapping suggests that $\beta_r \sim 7$ is a closer fit to the position and orientation of the

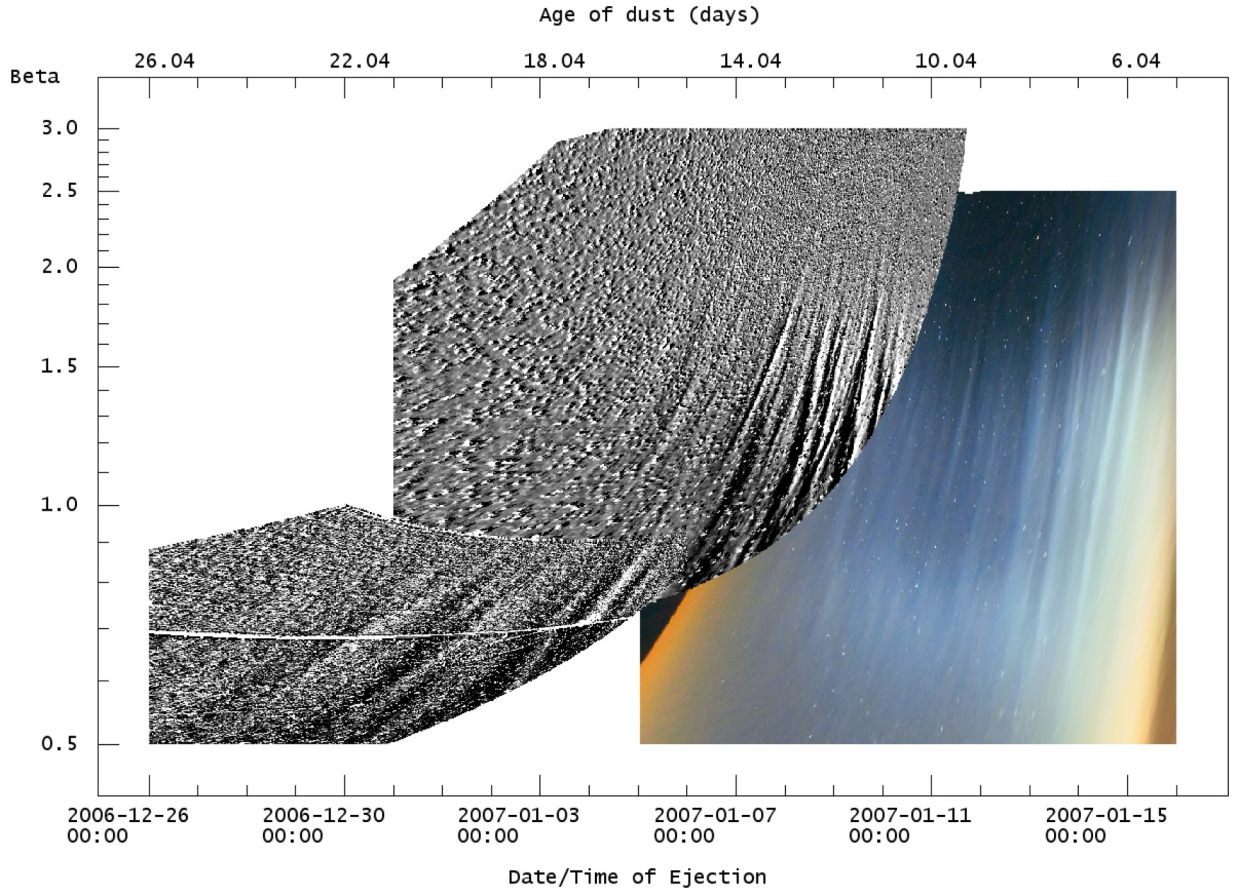

Fig. 8. Three week temporal map of the dust tail on January 21 at 01:00 UT, from STEREO HI-1 and HI-2 difference images and from Earth. This is a temporally mapped version of the mosaic shown in Fig. 7.

iron tail, as opposed to the value of $\beta_r \sim 6$ given by Fulle et al. (2007). The tail appears to be undetectable beyond an age of ~ 4.5 days. However, as the iron tail is a fast moving young feature compared to the main tail, it spreads over a large β_r range of 5.5 to 8.5. Additionally, like the main tail, the iron tail was also apparently striated. Vertical features in the temporal maps no more than two days old can be seen in these iron tail maps. These orientations are compatible with instantaneous release of material from the nucleus.

Mapping the region between the iron tail and main tail reveals a band of fainter, higher β_r striae, only visible in difference images. These reveal that many of the striae in the main tail extend from where $\beta_r \sim 1$, to higher values, often reaching $\beta_r \sim 8$, i.e. forming features that extend into the main portion of the iron tail.

Dust of β_r this high is not reported to be commonly observable (Fulle, 2004), or explainable by traditional theory (Burns et al., 1979), although considerations of the relatively recent *in situ* observations of fluffy dust aggregates by *Rosetta* instruments (e.g. Bentley et al., 2016) has yet to make its way into radiation pressure theory.

We propose several explanations for these features. These striae may form from a Sekanina or Nishioka type fragmentation process, which could release iron atoms contained within the parent dust. These atoms would then drift anti-sunward with a much higher β_r than observed in a typical striae, but wouldn't reach the iron tail proper, whose position is consistent with release from the nucleus, instead filling the gap between.

Alternatively, these very high β_r features may represent a continuum of even smaller grains. For very small particles approaching the wavelength scales of light, the relative magnitudes of forces for such small grains due to radiation pressure are smaller than for larger particles. That is, the effective β_r doesn't increase as rapidly as a function of decreasing size and concurrent increase in cross-sectional area:mass ratio. When grains become comparable in size to the wavelength of the solar photons impinging on them, radiation pressure becomes ineffective, as does the ability of very high β_r grains to scatter light.

4.4. Striae formation

Using the SOHO LASCO C3 Blue filter dataset, a sequence of 70 temporal maps was created. These maps cover the range $0.3 \leq \beta_r \leq 2.5$, from 2007 January 12 20:45 UT until January 15 18:45 UT. This sequence is available as an animation at the following link:

Striated features are clearly present, however due to the strong brightness gradient across the tail, they are difficult to track. The same sequence is presented again, with a simple unsharp mask applied to each frame by subtracting a Gaussian blurred version of the image. The unsharp masked sequence is available here:

A few frames from both sequences are shown in Fig. 12.

Remarkably, this sequence captures the formation of several striae; the authors believe that this is the first time that this process has been captured. From the features for which there are several days' worth of visibility, we explore the characteristics of formation for any clues on which mechanism might provide the best explanation.

Striated features appear to form in the dust approximately 2 to 2.5 days after release from the nucleus, assuming that the Finson-Probstein model is correct.

Visually, the striae usually form as juxtaposed regions that both brighten and darken. The smooth tail from which they form displays no sign of any detectable variations in brightness above background gradients. The appearance of features only reveals fully formed striae. We note that striae do not form in strict chronological order according to

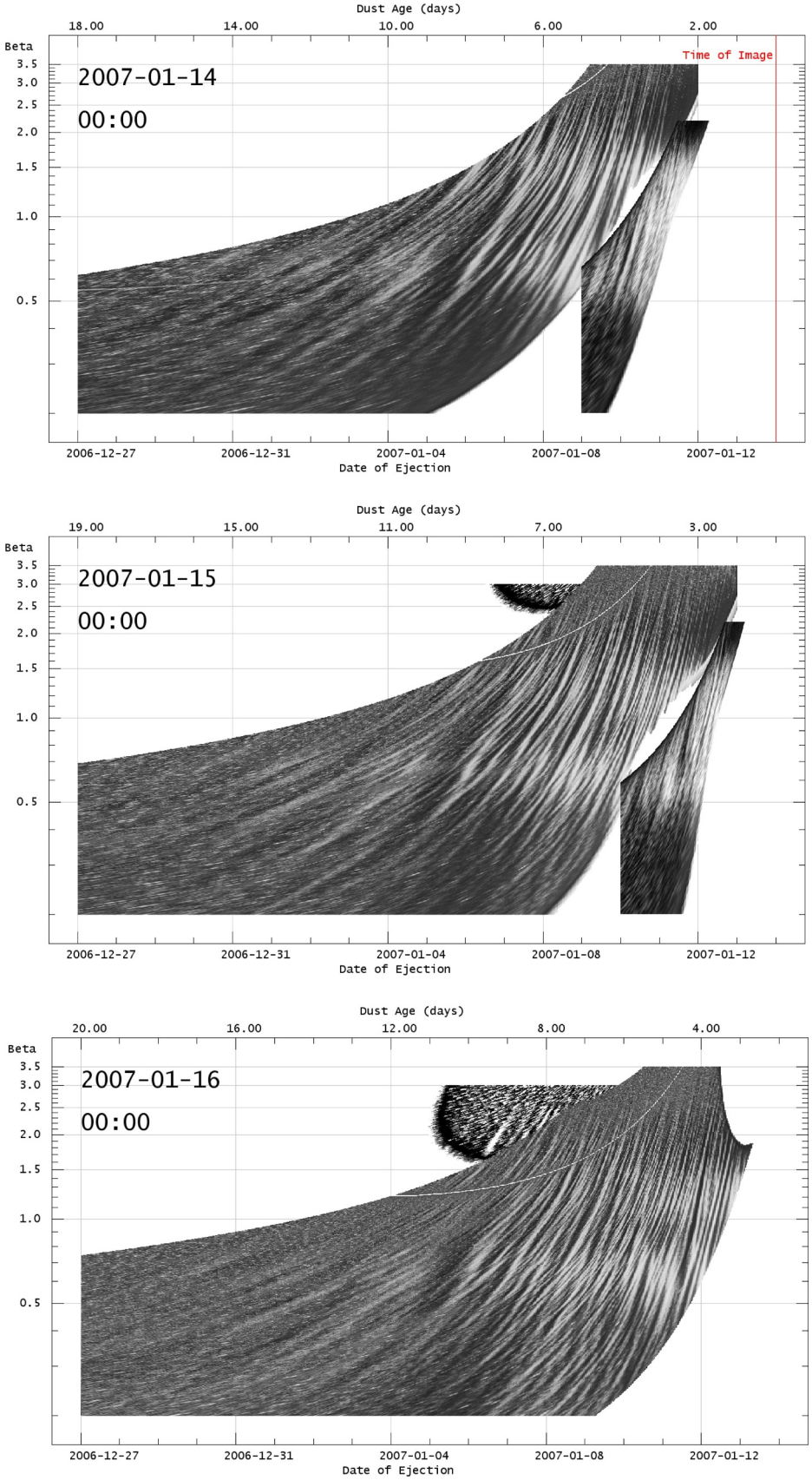

Fig. 9. Sequence of three temporal maps based on images taken 24 h apart, which show the progressive disruption and realignment of the striae in the dust tail.

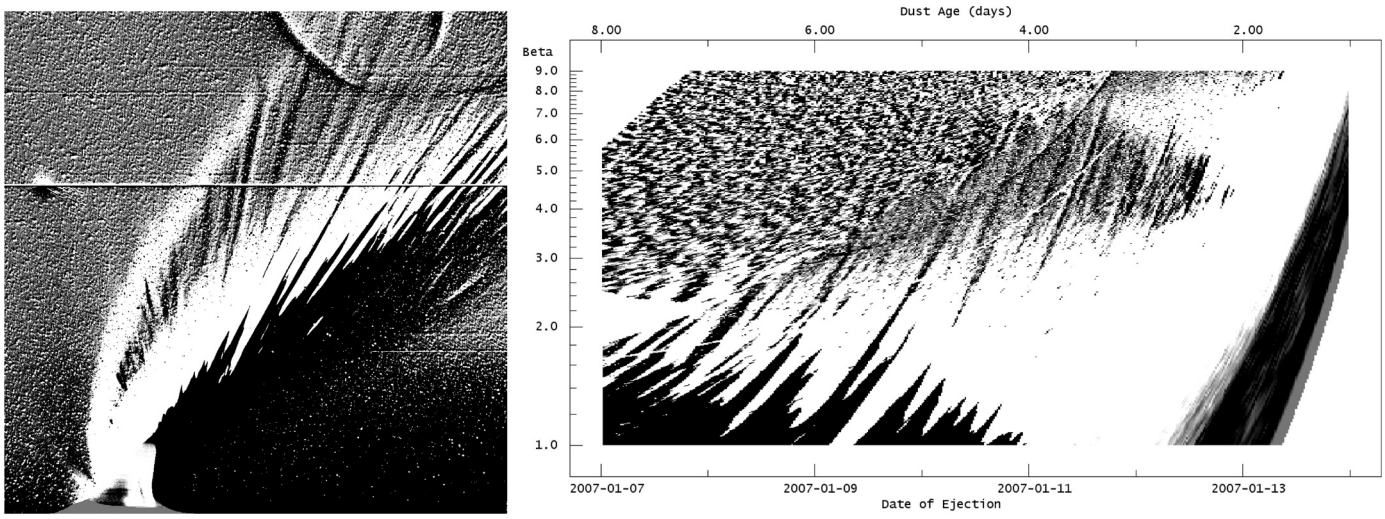

(a) STEREO-A HI-1 difference image. (b) Same image and concurrent HI-2 frame temporally mapped.

Fig. 10. Striae features between the main dust tail and iron tail on January 15 at 12:00 UT, accentuated through the use of the difference image technique. Panel (a) shows an original difference image from SECCHI-HI1. The upper tail is believed to be a neutral iron tail (Fulle et al., 2007). Near-linear features are seen to connect the main dust tail to the inferred iron tail for $\beta_r = 3$–7. Panel (b) shows the same image presented as a temporal map.

dust release; more prominent features seem to form from younger dust and may do so before all corresponding older dust has become striated. The observed formation is therefore suggestive of a rearrangement of existing dust, rather than of fragmentation occurring on a specific timescale.

Additionally we note that a particularly large gap forms from dust released up to and around midnight on January 12. This feature forms on the morning of January 14, as seen in Fig. 12, and remains notable throughout the LASCO C3 and STEREO-A HI-1 images taken after that time. We refer to this feature henceforth as the *notch*.

In order to understand precisely the role of solar radiation in the formation of these features, an additional mapping technique has been created for this sequence. We follow all the same steps as in Section 3.3, the only difference being that instead of plotting with t_e on the x-axis, we instead align features on this axis along radial sunward lines. To label these features, we refer to the time at which each sunward line would have been crossed by the comet nucleus. This sequence is available here:

A frame from this sequence and its original temporal map are shown in Fig. 13.

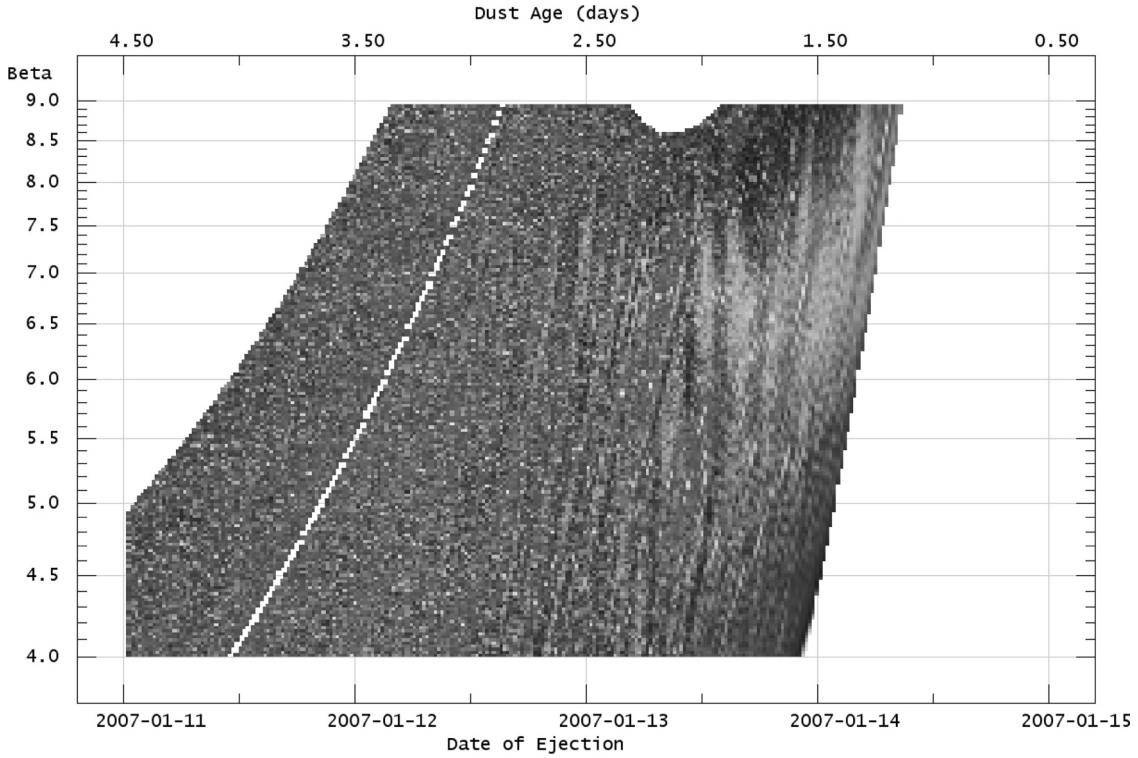

Fig. 11. Fine-scale structure in the iron tail as seen from STEREO-A HI-1. The vertical orientation of several January 13 features is consistent with abrupt release from the cometary nucleus on that date.

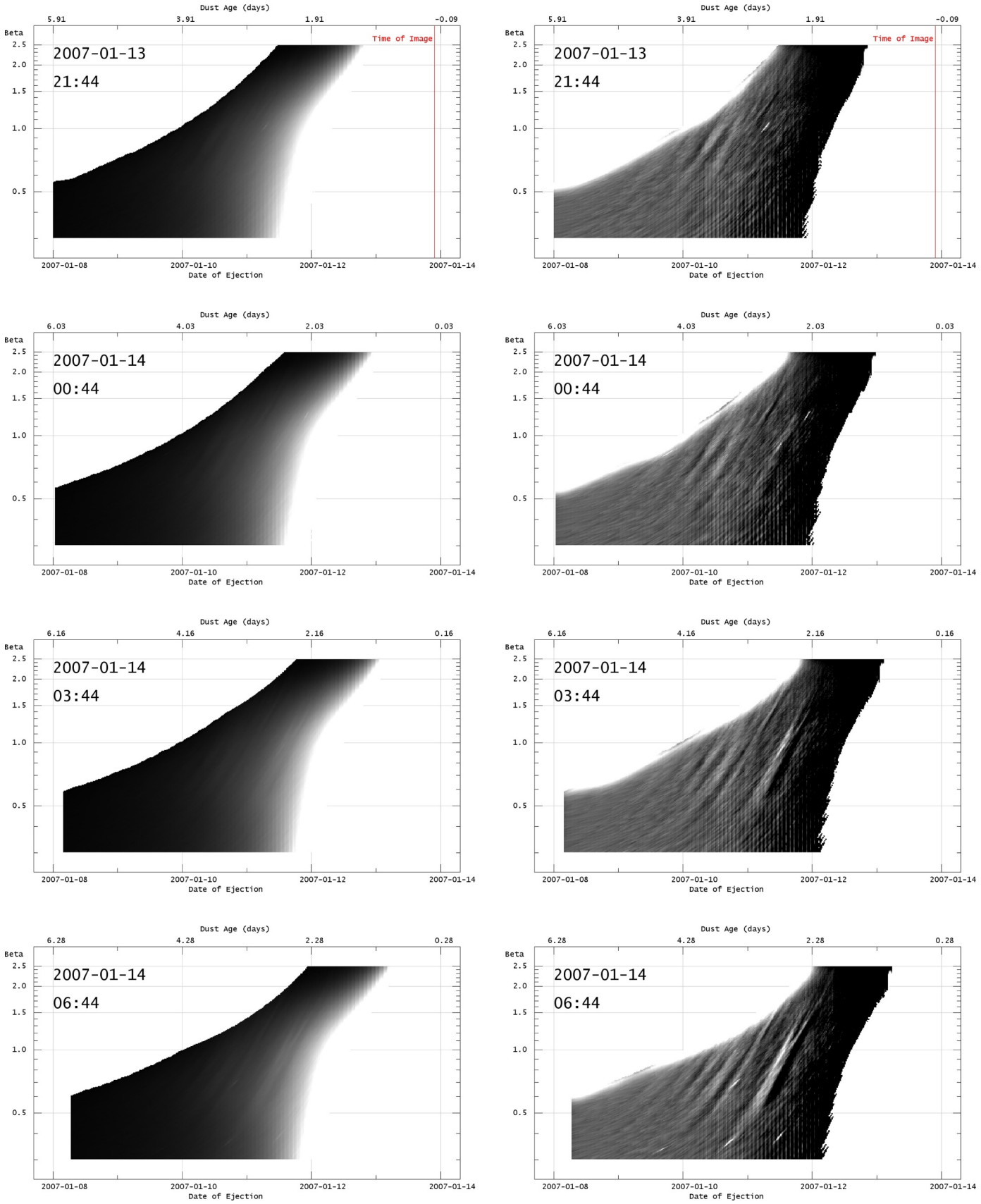

Fig. 12. A sequence of four pairs of temporal maps of the younger dust tail as seen in the SOHO LASCO C3 Blue filter datasets. The left images are temporal maps of the raw data, and the right images are the same temporal maps enhanced to show the structure. Across a 9 h period, structures form from dust released on the 11th January.

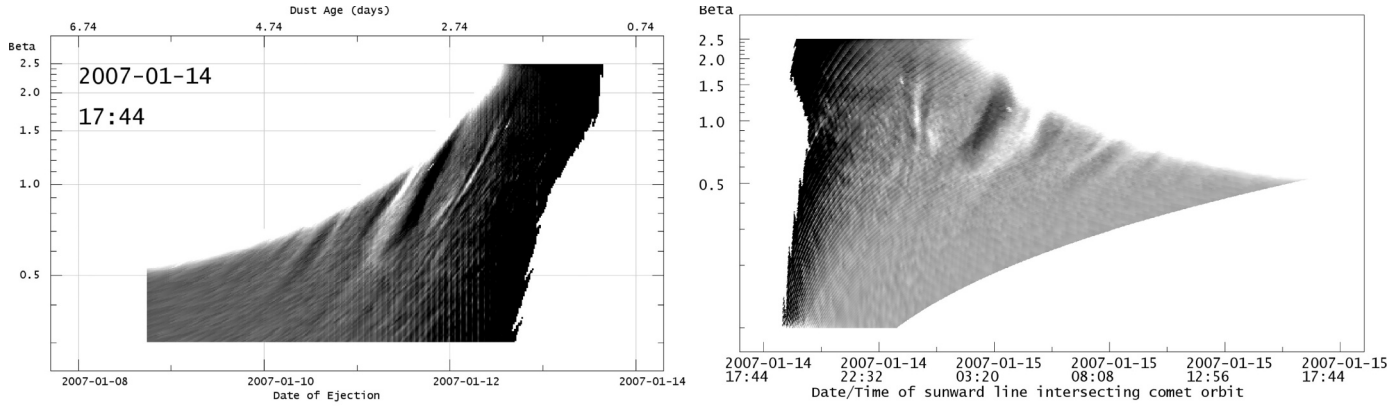

(a) Temporal Map (b) Sunward aligned Map

Fig. 13. Snapshot of striae formation observed by LASCO C3 with its Blue filter. A narrow stria is visible in the temporal map in panel (a) that has recently formed from dust released early on January 12. Panel (b) shows the same data projected such that each tail section is plotted against the time when the nucleus lay along the radial line from the Sun to the tail section. Features aligned with the local radial sunward direction will therefore appear vertical. The January 12 stria in (a) appears to be perfectly aligned with sunward, as do both of the dark lanes that formed either side of it. Note that time runs from left to right in panel (b), with the youngest tail regions on the left.

Studying the images taken by author M.D., we note that striae apparently continued to form many days after perihelion; Fig. 14 shows dust released on the January 20 still appears to display striated characteristics.

4.5. Striae disruption and reorganisation

Before the temporal mapping was applied to the STEREO-A HI-1 dataset, it was already clear that some process was disrupting the striae. Initially, the striae appeared at straight features as expected, as can be seen in Fig. 4. By January 16, many individual striae close to the nucleus had lost their distinct form. The younger tail section appeared more as a loose assortment of apparently *interleaved* striae-like features, shown in Fig. 15. The orientation of original striae can be loosely made out, as well as a secondary orientation of the disrupted features, which point roughly sunward.

Fig. 16 shows this change in structuring more clearly. In this image, the older striae still maintain their original morphology, however, later on they too become disrupted, and the disruption appears to commence at a fixed region in inertial space. This rearrangement of striae

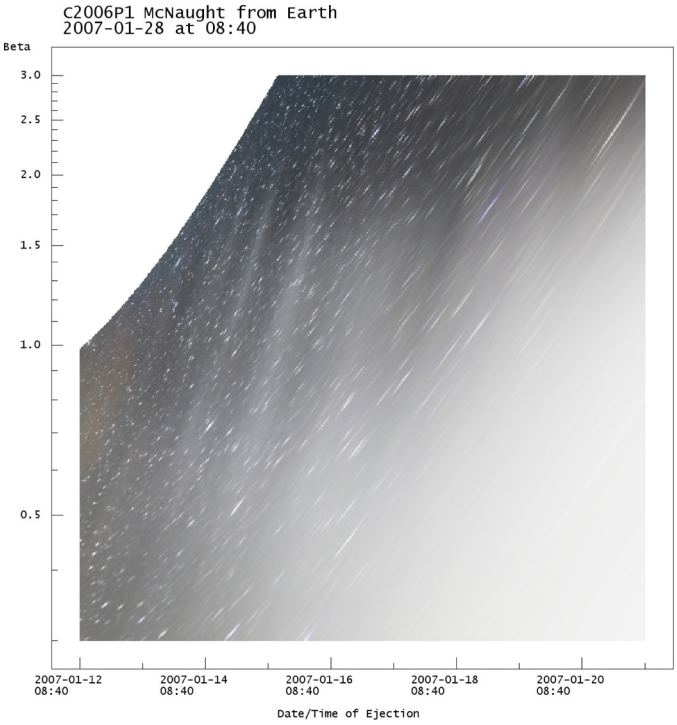

Fig. 14. Unenhanced temporal map of image taken in Argentina by author M.D., capturing the last striae observed to form to the authors' knowledge during McNaught's apparition. The "notch" is at the extreme left of this map.

Fig. 15. The tail of McNaught on 2007 January 16 at 00:01, as seen from HI-1 on STEREO-A. The nucleus has just left the field of view. At the younger end of the tail the striated form of the tail that was seen earlier (e.g. Fig. 4) has been replaced by striae-like features with a more disrupted appearance. The far end of the tail where the features are oldest still maintains its striated structure, although later it too becomes disrupted. The "notch" feature referred to in the text is visible at extreme lower left.

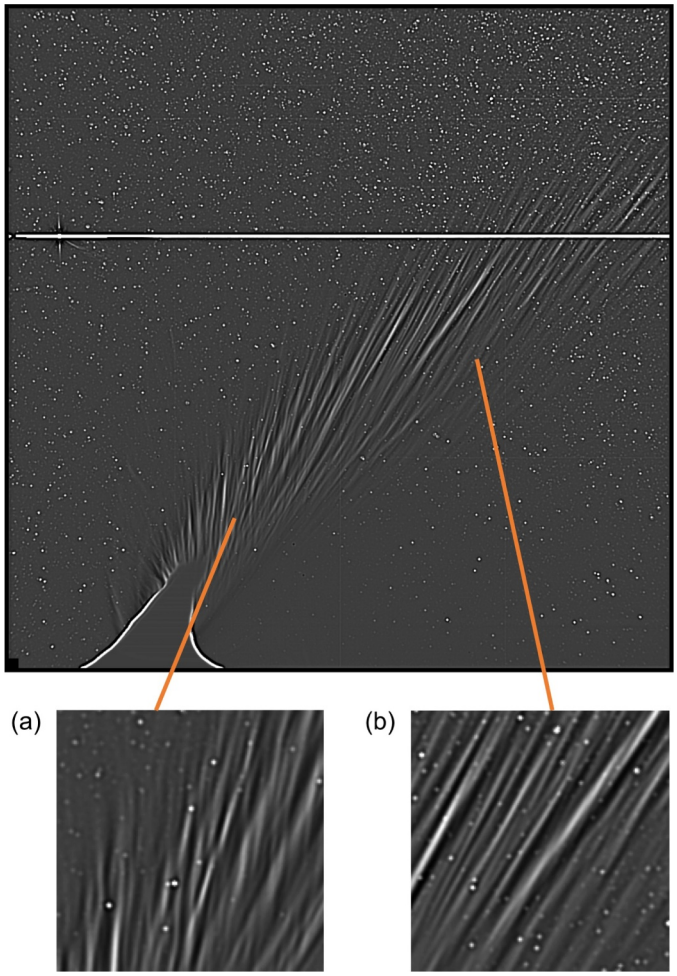

Fig. 16. The tail of McNaught on 2007 January 15 at 02:01 UT, as captured by HI-1 on STEREO-A, enhanced by subtracting a gaussian blurred version of the frame. The two insets show the clear difference between (a) the "interleaved" striae towards the south (left) part of the image, and (b) a region where striae remain largely near-parallel towards the north. The progression from near-aligned to interleaved spreads across the whole tail over time, as the comet moves towards the south.

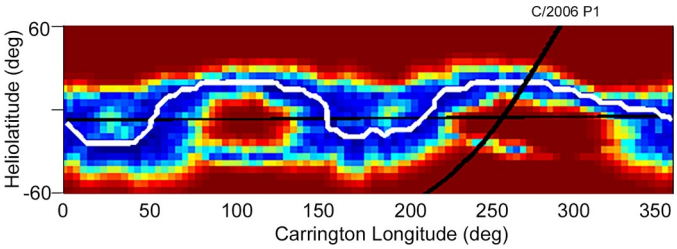

Fig. 17. A Mercator projection map of CORHEL modelled solar wind speeds for Carrington rotation 2052 - largely January 2007 - at a distance of 30 solar radii. Speeds range from 300 kms^{-1} (dark blue) to $\sim$ 750 kms^{-1} (red). The heliospheric current sheet, HCS, is traced by the white line. The thin black horizontal line shows the sub-Earth position during this solar rotation. McNaught's track is the inclined black line; motion was from north to south. McNaught entered the simulation domain at around 40 solar radii, reached perihelion at 36.7 solar radii on January 12. It then crossed the HCS, moving anti-sunward, and left the model domain at 70 solar radii. After crossing the HCS and surrounding streamer belt, the comet passed through an isolated region of slower solar wind. This fixed distance plot provides a general impression of the solar wind conditions encountered by McNaught. The parameter plots in Fig. 18 are more accurate, as they take the comet's changing heliocentric distance into account. (For interpretation of the references to colour in this figure legend, the reader is referred to the web version of this article.)

eventually affected all parts of the dust tail observed by SECCHI HI, including the parts further from the Sun only observed by HI-2. This progressive realignment, generally affecting younger dust first, and then the older material, rules out an explanation that the process is due to some kind of temporal dependence of the properties of the emitted dust, as might appear at first. The most likely explanation is therefore some kind of spatially-based one in which a localised phenomenon gradually affects the entire tail.

Before any further analysis can be done, the nature of the disruptive process must be better understood. This is hard to define purely from the original images, in a spatial and temporal sense, due to the transient motion and change in viewing conditions of the tail. We therefore targeted the development of the temporal mapping described here to allow for the precise description of this disruption process.

This is where the temporal map that we have created of the main tail becomes important (Fig. 9):

As was mentioned, this gives a view of the main dust tail where $0.2 \leq \beta_r \leq 3$, which is the affected region. By utilising multiple datasets we can gather a two week picture from 2007 January 11 00:00 UT, before any disruption has occurred, until January 25 02:00 UT, well after the disruption begins, allowing us to see how it permanently affects the tail structure.

From the inspection of this temporal map sequence, more conclusions can be drawn about the disruptive process, and the form of the reorganisation process is immediately more clear. The bright stria with $\beta_r = 1$ for dust released on January 9 in Fig. 9 provides a good example. On midnight on January 14 it has just started to be affected, appearing still as a definite feature with some variation. One day later, the disruption has started to occur to the lower β_r dust in the striae, forming some interleaved striae. This takes the form of thin, striated features which appear to transect the pre-existing striae at a different angle. After another day, the stria no longer exists as a continuous structure, instead appearing as a feature comprised of many different sections of interleaved striae.

Unfortunately there are some limitations of the mapping accuracy at the beginning of the sequence. The slightly imperfect astrometric data of the original STEREO-A HI files during instrument commissioning means that features on January 11 and 12 move around slightly in the temporal maps. This motion is strictly non physical, and is only due to inconsistencies in the FITS metadata during the beginning of the temporal sequence. Additionally, as this dust is younger and the tail fills less of the HI-1 field of view, there is a sharpening of features as the tail expands and the sampling rate of the mapping improves. Finally there is a six hour data gap between 16:00 and 22:00 on January 12.

These effects mean that it is hard to pinpoint the exact time at which reorganisation starts within the striae. At best, we can say that global striae reorganisation is first observed definitively on January 13, when the first of the interleaved striae are seen. The reorganization appears to begin at a fixed region in inertial space, i.e. consistent with a change in the space environment which the comet and its tail are traversing.

4.6. Evidence of solar wind effects

The most obvious candidate for a cause of the strong localised striae reorganisation is the variation in the solar wind conditions at the comet. To investigate the likely solar wind conditions at McNaught, we extracted the modelled conditions nearest to the comet's nucleus in the CORHEL inner heliosphere MHD simulation (Odstrcil et al., 2004), for Carrington Rotation 2052 (2007 January 8 to February 4). The model run employed solar magnetogram data from both SOLIS and the Wilcox Solar Observatory (the latter not shown). Due to its high orbital inclination, McNaught was only within the $\pm$ 60° heliolatitude simulation domain during 2007 January 11 to 19.

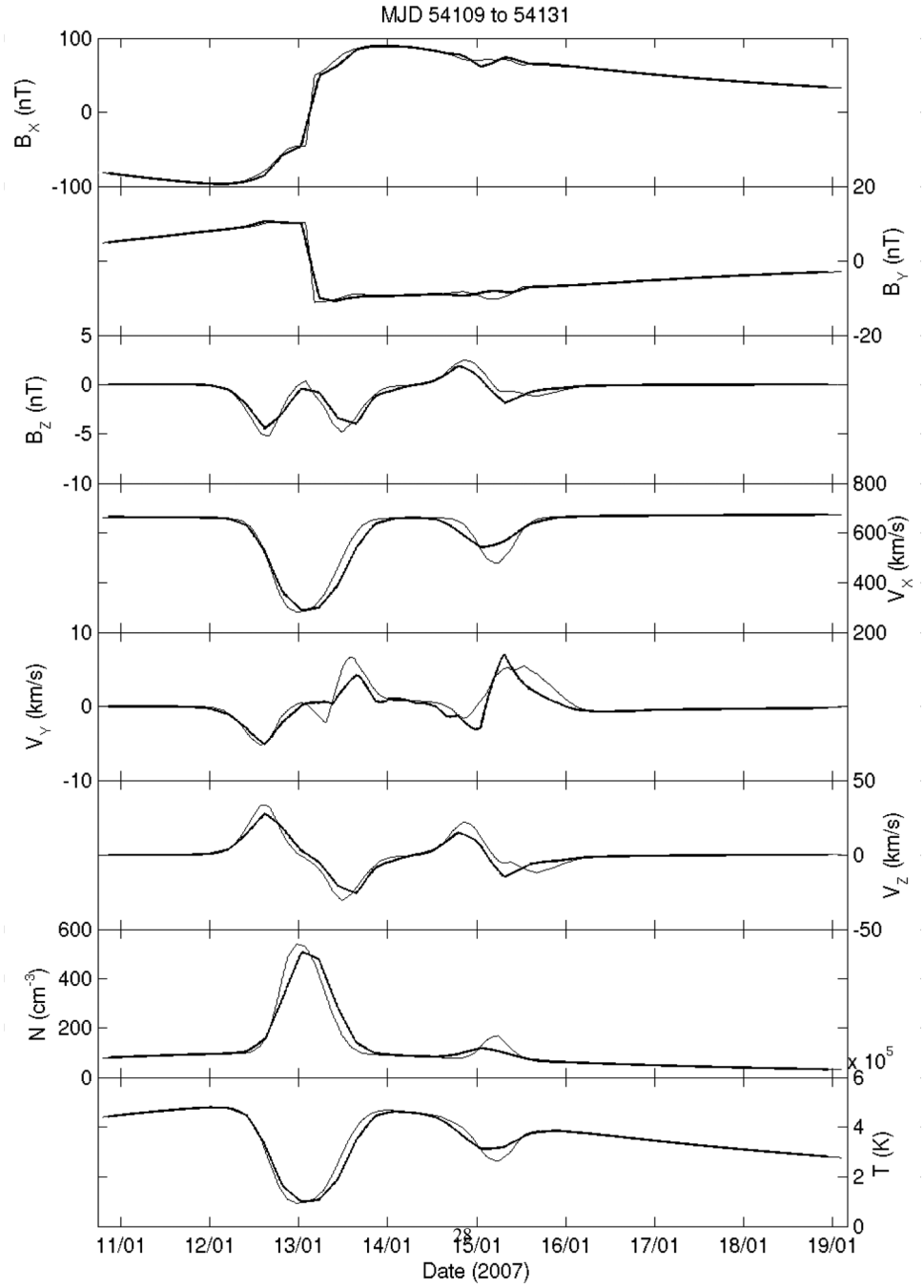

Fig. 18. Solar wind conditions at the nucleus of McNaught estimated using the CORHEL model, extracted along the path of McNaught in Fig. 17, plotted against date in the format month/day. From top to bottom, the panels show the three components of the heliospheric magnetic field in the Radial-Tangential-Normal coordinate system; three components of the solar wind speed in the same system, the solar wind particle number density, and finally the plasma temperature. The black and grey lines correspond to the two solar magnetogram datasets used.

The global corona is modelled by the Magnetohydrodynamics Around a Sphere (MAS) 3D MHD code (Linker et al., 1999; Mikić et al., 1999). Photospheric magnetic field observations provide the boundary conditions, from which initial conditions are derived by a potential field solution to the photospheric radial field, a uniform boundary density and a Parker-type solar wind outflow. The MAS coronal solution acts as a boundary condition for the heliospheric model, in this case the ENLIL 3D ideal MHD code developed at NOAA/SEC, e.g., Odstrcil (2003), and references therein. ENLIL's standard computational domain covers 30 solar radii to 1 AU, and -60° to $+60^{\circ}$ in solar latitude. See Odstrcil et al. (2004) and Luhmann et al. (2004) for details of the code coupling. The heliospheric solution was allowed to relax to a steady state.

The CORHEL results, using SOLIS input data, are presented in Figs. 17 and 18. The results based on both SOLIS and Wilcox Solar Observatory data (the latter not shown in Fig. 17, but qualitatively similar) imply a clear change in solar wind conditions centred on early January 13, when the nucleus crossed the heliospheric current sheet, HCS, that separates regions of opposite heliospheric magnetic field polarity. McNaught crossed from the northern hemisphere's then inward magnetic polarity to the southern outward polarity (Fig. 19).

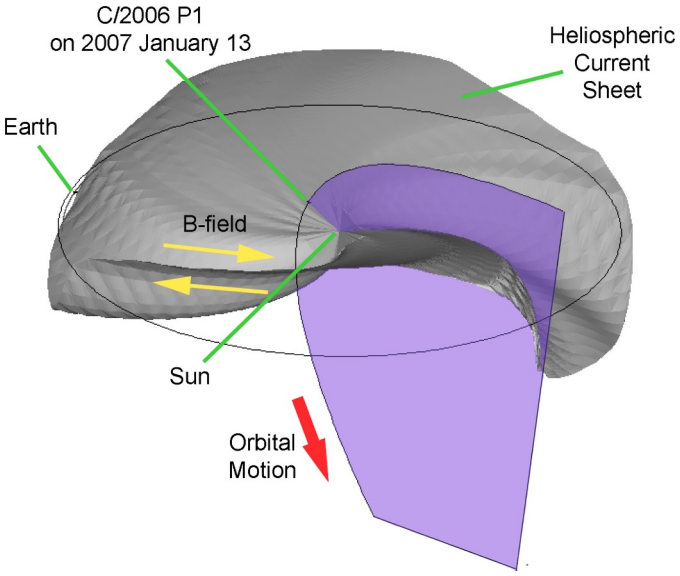

Fig. 19. The relative positions of Comet McNaught's orbit and the heliospheric current sheet, HCS, as estimated from the CORHEL model. Yellow arrows denote the general direction of the heliospheric magnetic field to the north and south of the HCS. Earth's orbit at 1 AU from the Sun is shown as a circle. The HCS, comet nucleus, and planet's positions are shown for 2007 January 13. (For interpretation of the references to colour in this figure legend, the reader is referred to the web version of this article.)

Around the HCS crossing were solar wind plasma changes associated with the comet crossing the streamer belt, including a drop in plasma temperature, a significant increase in solar wind number density, and a drop in solar wind speed. A second, more modest period of varying solar wind conditions was centred on early January 15, visible in Fig. 17 as a region of slower solar wind associated with a large equatorial active region at Carrington longitude $\sim 245^{\circ}$. The clear correlation between the obvious changes in the striae orientation and the crossing of the HCS by McNaught presents, in our opinion, a persuasive case that the dust grains in McNaught's tail show clear evidence of an interaction between the solar wind and comet. The most obvious reason for such an observable change coincident with the HCS crossing is the expected large change in the Lorentz force acting on electrically charged particles. The Lorentz force is associated with the motional electric field generated by the solar wind flow past the comet. A reversal in heliospheric magnetic field direction associated with a HCS crossing would result in a potentially dramatic change in direction of the Lorentz force. Electrically charged grains south of the HCS would therefore be accelerated in a different direction to that induced by the Lorentz force direction north of the HCS. Such an observable effect associated with a HCS crossing was predicted by Horanyi and Mendis (1987), and described more recently by Mendis and Horányi (2013).

Kramer et al. (2014) inferred an observable effect on charged dust in the tail of C/1996 O1 (Hale-Bopp) when at large heliocentric distances. Finding a dust tail at surprisingly large heliocentric distances of 21.6 and 27.2 AU, they found the Finson-Probstein model alone to be insufficient to explain even the basic orientation of the tail. Out of several candidate forces, they found the Lorentz force the best explanation for the shape, inferring its importance to dust dynamics at high heliocentric distances. This is due to the Lorentz force having only a r^{-1} dependence with heliocentric distance. Whilst we are dealing here with small heliocentric distances, the result that the dust is charged strongly enough for its motion to be affected is important.

We regard a comprehensive study of the changing solar wind effects on the comet as being outside the scope of this paper, and we therefore defer such a study to a later publication. Several complicating factors in understanding the nature of the dust-solar wind interactions include the fact that the estimated solar wind conditions that we can easily derive are those for the comet's head only, whereas the striae which are observed to change in orientation are up to 0.4 AU further away from the Sun. We also note that the HCS is distorted at a comet's head due to magnetic field line-draping; dust particles in the coma in particular will therefore have likely encountered a complex magnetic field structure, not a relatively simple reversal of magnetic field direction. In addition, as local undulations in the HCS may exist, and as the line of intersection between the comet's orbit and the HCS is gradually changing with the rotation of the sun and the propagation of solar wind structures, the exact locations in inertial space where the Lorentz force is modified in the tail may be changing with time.

It is possible to estimate the comparative magnitude of a Lorentz force to radiation pressure and gravity. At an average position in the tail at a heliocentric distance of 0.25 AU, this is roughly:

$$a_{FP} = \frac{(1-\beta_r)GM_{\odot}}{r^2} \approx (1-\beta_r)\,0.1 ms^{-2} \tag{4}$$

The Lorentz force can be formulated as:

$$\vec{a}_{Lorentz} = \frac{q}{m}[(\vec{v}_{dust} - \vec{v}_{sw}) \times \vec{B}] \tag{5}$$

The solar wind speed $\vec{v}_{sw}$ dominates above the dust speed $\vec{v}_{dust}$ and so the azimuthal component of the magnetic field is the most important component. The charge to mass ratio can be related to β_r (Kramer et al., 2014):

$$\frac{q}{m} = \frac{12\varepsilon_0 V}{C^2}\beta_r^2 \frac{\rho_d}{Q_{pr}^2} \tag{6}$$

Allowing for an estimate of the magnitude of the Lorentz force to be made:

$$a_{Lorentz} = \frac{12\varepsilon_0 V}{C^2}\beta_r^2 \frac{\rho_d}{Q_{pr}^2} B_{\phi} v_{sw} \tag{7}$$

Assuming dust is charged to $+5$V, with $\rho_d = 1000$ kg m^{-3} and $Q_{pr} = 1$, taking the values of $B_{\phi} = 10$ nT and v_{sw}= 300 kms^{-1} from Fig. 18, and using the constant $C = 5.76 \times 10^{-4}$ kg m^{-2}, we can obtain a guess for the magnitude of the Lorentz force as:

$$a_{Lorentz} = \beta_r^2\, 0.005 ms^{-2} \tag{8}$$

Hence, assuming a continuous Lorentz force acting on the dust when the comet was still north of the current sheet and associated streamer belt, at the HCS crossing where we see a change from B_{ϕ} from 10 nT to -10 nT, the orientation change of the Lorentz force may account for a sudden perturbation in the motion of the dust. This could be at least 10% the magnitude of gravity and radiation pressure, and higher for high β_r dust, which is easily enough to affect the dynamics of the dust. The implication that the Lorentz force clearly has observable effects – that may only become readily apparent when the strength and/or direction of that force changes – should be included in any future comprehensive studies of cometary dust dynamics. We note that Kimura et al. (1985) concluded that the behaviour of striae in C/1957 P1 (Mrkos) and C/1975 V1 (West) implied the presence of non-radial perturbations which they concluded were most likely Lorentz forces, with a more general discussion of solar wind effects on dust at comets being also discussed around that time by Ip et al. (1985).

The implications of the Lorentz force's observable effects include a complication in the interpretation of striae. Once the comet crossed the current sheet, there were three "families" of dust present in the tail:

1. those released prior to crossing the HCS, and still north of the HCS, and unperturbed by any change in the motional electric field
2. those released prior to crossing the HCS, but had subsequently crossed the HCS during which time their dynamical behaviour has been altered

3. those released after HCS crossing, in a "new" near-steady magnetic field regime, and hence unaffected by changes during the HCS crossing itself

A careful future study of the relative behaviour of these three families of particles could provide useful constraints on the magnitude of the forces involved, and could in turn improve our understanding of the relationship between the inherent β_r value of dust grains, their actual masses, and their cross-sectional area to radiation pressure.

In future studies of these effects, it should also be borne in mind that changes in the dynamic pressure of the solar wind may also be detectable, e.g. Gustafson (1994) and Minato et al. (2004), especially when reasonably close to the Sun where the solar wind number density is relatively high. We note that the formation of the prominent "notch" feature so close to the time when the nucleus was apparently crossings the HCS may be related to the then-rapidly changing solar wind conditions at the comet's head.

4.7. Striae lifetime

The extended observational dataset used here allows individual striae to be tracked for longer than in previous studies that were based on much smaller ground based datasets. This enabled us to study the longevity of the striae; in particular using the STEREO-A HI-1 and HI-2 datasets, and also loosely relate the dependence of these lifetimes on β.

Striae remain visible in both maps when studying difference images, although the signal to noise ratio at times is extremely poor due to the noise associated with the moving background starfield. A statistical extraction of the signal is therefore difficult and we are therefore reliant on the somewhat flawed method of visual inspection. In particular we run into two observational biases: we *expect* to see features and may be convinced that we can see some after they may have actually disappeared, and we may have a heightened ability to see *moving* features.

This leads to a discrepancy between methods of study. Looking at individual temporal mapped frames, striated features in STEREO-A HI-1 data remain just visible until around midday on January 22, and those in HI-2 can be seen until midday on the 27th. Looking however at an animation of the original difference enhanced FITS images, the relative motion of the striae actually allows our eyes to continue to perceive the presence features for a few extra days, in HI-1 until January 24 and HI-2 until the 30th.

The temporal maps do allow for the original release times of the released striae material and their β ranges to be read off easily and these can be cross referenced with the original images to work out which are the longest surviving striae. The oldest HI-1 features are at $0.5 \leq \beta \leq 0.8$ and date back to midday on 2006 December 29, meaning the oldest features are just over 26 days old. In HI-2, the longest lasting striated features are at $1.2 \leq \beta \leq 1.8$ and were formed on January 7 to 8, making them 23 days old. These two samples roughly represent the two peaks of the bimodal dust distribution.

For the material within the iron tail, lifetimes are much shorter than in the main dust tail, with features disappearing from temporal maps within 5 days. If this material is indeed composed of iron atoms, then this is controlled by the atoms' photoionization lifetime, as studied by Fulle et al. (2007). If grains exist in this tail, then this inverse relation of apparent lifetime to β may be mainly due to higher β features spreading out more quickly and reducing in surface brightness faster than the main dust tail. There may also be some dependence on increased fragmentation and destruction by sublimation of smaller grain sizes.

5. Conclusions and discussion

5.1. The temporal mapping technique

The temporal mapping technique, published here for the first time, has proven itself to be a very useful method for the direct analysis of cometary dust tails. It allows for effects of physical scale, transient motion and observer geometry to be removed, and has enabled us to combine and investigate numerous images of McNaught from different sources. This co-mapping has proven to be very successful, with tail features remaining steady at the fixed formation age-β_r location in phase space. The authors plan to apply this analysis method to other comets in the future.

5.2. Dust-solar wind interactions

The McNaught observations confirm that solar wind conditions can have a significant effect on observable dust tail structure. We believe that the most likely cause of the observed effects are due to changes in the Lorentz force, as previously predicted (Horanyi and Mendis, 1987). One puzzling aspect of the striae rearrangement associated with the HCS crossing is that the effect is observable at all. It has been known for many years that charged dust grains' trajectories can be affected by Lorentz forces, but these have only been observed previously by *in situ* observations in various solar system contexts, e.g. Strub et al. (2015); Hsu et al. (2011), and these populations have been generally regarded as being too small for remote observation in the visible range.

For example, studies of Jupiter's gossamer ring particles with the *Galileo* spacecraft dust detector revealed the presence of high inclination grains down to ~ 0.3 μm in scale that were not visible in images of the same ring (Hamilton and Krüger, 2008), where particles only a few μm across and larger were detectable. The observations presented here, together with those of Kramer et al. (2014), imply that grains strongly susceptible to electrodynamic forces are larger than had been previously anticipated. The authors plan to make quantitative estimates of the masses and effective areas of these grains as part of a future study.

5.3. Striae formation

Assuming that our interpretation of the solar wind interaction is correct, some aspects of the observed changes in the striae on crossing the HCS can help provide constraints on the proposed striae formation processes.

If the Sekanina and Farrell (1980) two-step formation process is responsible for striae, then each stria would contain a progressively higher β_r with increasing distance from the Sun, hence the regions of striae farthest from the Sun would exclusively contain the highest β_r (generally lowest mass) grains. In this situation, the furthest extremities of the striae would therefore be most susceptible to the Lorentz force, and to changes to it, hence to a HCS crossing.

If instead the Nishioka (1998) "cascade" striae formation process is operating, each stria would contain a more homogeneous distribution of β_r values along its length, as a result of multiple fragmentation events leading to the formation of each linear structure. Crossing the HCS with this β_r distribution would lead us to expect disruption to occur throughout the length of a stria on the reversal in polarity of the heliospheric magnetic field, and hence a change in the Lorentz force direction.

The appearance of "interleaved" striae after the HCS crossings is certainly in better agreement with the latter scenario, with multiple regions along each stria showing a displaced portion. Our analysis strongly suggests that Nishioka's "cascade" model best fits the observations, and that striae are not formed in single fragmentation events, at least for Comet McNaught.

The mechanism detailed by Froehlich and Notni (1988) also explicitly considers the co-existence of multiple β_r dust along the striae due to optical thickness effects. They claim that higher relative β_r particles may exist on one side a cloud furthest from the sun, with lower β_r particles existing on the near side. Although Steckloff and Jacobson (2016) do not make any such definitive statements, we note that due to the cascading formation of striae it should allow for these "interleaved" striae to be present.

We again note the remarkable sequence of stria formation recorded by LASCO and presented in Section 4.4. Each stria appears to essentially form as a largely complete region which suddenly brightens over 6–9 h. If a Sekanina or Nishioka type formation process was occurring, the striae would form from parent particles of a small range of β_r, and would then spread out as the daughter particles distinguished themselves by their characteristic β_r. There is little observational evidence to suggest a mechanism where they extend in β_r as time progresses, except perhaps at the high and low β_r ends of the striae.

Some striae appear to form almost perfectly aligned with the radial direction from the sun, a good example highlighted earlier in Fig. 13. Many such striae also form in conjunction with dark lanes adjacent to the striae, giving the appearance of material being swept together to form striae. These effects are both consistent with, and appear to hint towards the role of optical thickness and shadowing mechanisms having importance in the formation of some striae, as detailed in Froehlich and Notni (1988).

Striae do not form chronologically with dust ejection time. This is quite well explained by the high variability in the "Sublimation-YORP", or SYORP, timescales proposed in the work of Steckloff and Jacobson (2016), although it is not strictly forbidden by any of the other mechanisms.

As the directly-observed stria formation took place during January 15, when from the CORHEL model we expect that the comet was undergoing changes in its solar wind environment, we tentatively speculate that those particular striae may be formed through a change in the comet's solar wind conditions, rather than through a fragmentation-only process that may be responsible for many, if not most, of these spectacular structures.

Acknowledgements

OP is supported by a UK Science and Technology Facilities Council (STFC) PhD studentship. GHJ is grateful to STFC for partial support through consolidated grants ST/K000977/1 and ST/N000722/1. KB is supported by the NASA-Funded Sungrazer Project; grant number NNG12PP90I. *Astrometry.net* is funded by the US National Science Foundation, the US National Aeronautics and Space Administration NNG12PP90I, and the Canadian National Science and Engineering Research Council. The SOHO/LASCO data used here are produced by a consortium of the Naval Research Laboratory (USA), Max-Planck-Institut für Sonnensystemforschung (Germany), Laboratoire d'Astronomie (France), and the University of Birmingham (UK), and are available via https://sohowww.nascom.nasa.gov/data/. SOHO is a project of international cooperation between ESA and NASA. The STEREO/SECCHI data are produced by an international consortium of the NRL (USA), LMSAL (USA), NASA-GSFC (USA), RAL (UK), University of Birmingham (UK), MPS (Germany), CSL (Belgium), IOTA (France), and IAS (France), and are available via https://stereo-ssc.nascom.nasa.gov/. SOLIS magnetograms are produced cooperatively by NSF/NSO and NASA/LWS. The National Solar Observatory (NSO) is operated by the Association of Universities for Research in Astronomy, Inc., under cooperative agreement with the National Science Foundation. This research made use of Astropy, a community-developed core Python package for Astronomy (Astropy Collaboration, 2013).

References

Astropy Collaboration, 2013. Astropy: a community Python package for astronomy. Astron. Astrophys. 558, A33.

Battams, K., Knight, M.M., 2017. SOHO comets: 20 years and 3000 objects later. Philos. Trans. R. Soc. A 375 (2097), 20160257. https://doi.org/10.1098/rsta.2016.0257.

Bentley, M.S., Schmied, R., Mannel, T., Torkar, K., Jeszenszky, H., Romstedt, J., Levasseur-Regourd, A.-C., Weber, I., Jessberger, E.K., Ehrenfreund, P., Koeberl, C., Havnes, O., 2016. Aggregate dust particles at comet 67P/Churyumov-Gerasimenko. Nature 537 (7618), 73–75. https://doi.org/10.1038/nature19091.

Bewsher, D., Brown, D.S., Eyles, C.J., Kellett, B.J., White, G.J., Swinyard, B., 2010. Determination of the photometric calibration and large-scale flatfield of the STEREO heliospheric imagers: I. HI-1. Solar Phys. 264 (2), 433–460. https://doi.org/10.1007/s11207-010-9582-8.

Brueckner, G., Howard, R., Koomen, M., Korendyke, C., Michels, D., Moses, J., Socker, D., Dere, K., Lamy, P., Llebaria, A., et al., 1995. The large angle spectroscopic coronagraph (LASCO). Solar Phys 162 (1–2), 357–402.

Burns, J.A., Lamy, P.L., Soter, S., 1979. Radiation forces on small particles in the solar system. Icarus 40 (1), 1–48. https://doi.org/10.1016/0019-1035(79)90050-2.

Combi, M.R., Boyd, Z., Lee, Y., Patel, T.S., Bertaux, J.-L., Quémerais, E., Mäkinen, J.T.T., 2011. SOHO/SWAN observations of comets with small perihelia: C/2002 V1 (NEAT), C/2002 X5 (Kudo-Fujikawa), 2006 P1 (McNaught) and 96P/Machholz 1. Icarus 216, 449–461. https://doi.org/10.1016/j.icarus.2011.09.019.

Eyles, C., Harrison, R., Davis, C., Waltham, N., Shaughnessy, B., Mapson-Menard, H., Bewsher, D., Crothers, S., Davies, J., Simnett, G., et al., 2009. The heliospheric imagers onboard the STEREO mission. Solar Phys. 254 (2), 387–445.

Finson, M., Probstein, R., 1968. A theory of dust comets. I. Model and equations. Astrophys. J. 154, 327–380. https://doi.org/10.1086/149761.

Froehlich, H.-E., Notni, P., 1988. Radiation pressure a stabilizing agent of dust clouds in comets? Astron. Nachr. 309 (2), 147–155. https://doi.org/10.1002/asna.2113090211.

Fulle, M., 2004. Motion of cometary dust. pp. 565–575.

Fulle, M., Leblanc, F., Harrison, R.A., Davis, C.J., Eyles, C.J., Halain, J.P., Howard, R.A., Bockelée-Morvan, D., Cremonese, G., Scarmato, T., 2007. Discovery of the atomic iron tail of comet McNaught using the Heliospheric Imager on STEREO. Astrophys. J. Lett. 661, L93–L96. https://doi.org/10.1086/518719.

Giorgini, J.D., Yeomans, D.K., Chamberlin, A.B., Chodas, P.W., Jacobson, R.A., Keesey, M.S., Lieske, J.H., Ostro, S.J., Standish, E.M., Wimberly, R.N., 1997. JPL's on-line solar system ephemeris and data service. In: Bietenholz, M.F., Bartel, N., Rupen, M.P., Beasley, A.J., Graham, D.A., Altunin, V.I., Venturi, T., Umana, G., Conway, J.E. (Eds.), Bulletin of the American Astronomical Society. Bulletin of the American Astronomical Society 29. pp. 1099.

Gustafson, B.A.S., 1994. Physics of zodiacal dust. Annu. Rev. Earth Planet. Sci. 22, 553–595. https://doi.org/10.1146/annurev.ea.22.050194.003005.

Hamilton, D.P., Krüger, H., 2008. The sculpting of Jupiter's gossamer rings by its shadow. Nature 453 (7191), 72–75. https://doi.org/10.1038/nature06886.

Hilchenbach, M., Kissel, J., Langevin, Y., Briois, C., von Hoerner, H., Koch, A., Schulz, R., Silén, J., Altwegg, K., Colangeli, L., Cottin, H., Engrand, C., Fischer, H., Glasmachers, A., Grün, E., Haerendel, G., Henkel, H., Höfner, H., Hornung, K., Jessberger, E.K., Lehto, H., Lehto, K., Raulin, F., Le Roy, L., Rynö, J., Steiger, W., Stephan, T., Thirkell, L., Thomas, R., Torkar, K., Varmuza, K., Wanczek, K.-P., Altobelli, N., Baklouti, D., Bardyn, A., Fray, N., Krüger, H., Ligier, N., Lin, Z., Martin, P., Merouane, S., Orthous-Daunay, F.R., Paquette, J., Revillet, C., Siljeström, S., Stenzel, O., Zaprudin, B., 2016. Comet 67P/Churyumov-Gerasimenko: close-up on dust particle fragments. Astrophys. J. Lett. 816, L32. https://doi.org/10.3847/2041-8205/816/2/L32.

Hill, J.R., Mendis, D.A., 1980. On the origin of striae in cometary dust tails. Astrophys. J. 242, 395–401. https://doi.org/10.1086/158472.

Horanyi, M., Mendis, D.A., 1987. The effect of a sector boundary crossing on the cometary dust tail. Earth Moon Planets 37, 71–77. https://doi.org/10.1007/BF00054325.

Howard, R.A., Moses, J.D., Vourlidas, A., Newmark, J.S., Socker, D.G., Plunkett, S.P., Korendyke, C.M., Cook, J.W., Hurley, A., Davila, J.M., Thompson, W.T., St Cyr, O.C., Mentzell, E., Mehalick, K., Lemen, J.R., Wuelser, J.P., Duncan, D.W., Tarbell, T.D., Wolfson, C.J., Moore, A., Harrison, R.A., Waltham, N.R., Lang, J., Davis, C.J., Eyles, C.J., Mapson-Menard, H., Simnett, G.M., Halain, J.P., Defise, J.M., Mazy, E., Rochus, P., Mercier, R., Ravet, M.F., Delmotte, F., Auchere, F., Delaboudiniere, J.P., Bothmer, V., Deutsch, W., Wang, D., Rich, N., Cooper, S., Stephens, V., Maahs, G., Baugh, R., McMullin, D., Carter, T., 2008. Sun Earth Connection Coronal and Heliospheric Investigation (SECCHI). Space Sci. Rev. 136, 67–115. https://doi.org/10.1007/s11214-008-9341-4.

Hsu, H.-W., Kempf, S., Postberg, F., Trieloff, M., Burton, M., Roy, M., Moragas-Klostermeyer, G., Srama, R., 2011. Cassini dust stream particle measurements during the first three orbits at Saturn. J. Geophys. Res. (Space Phys.) 116, A08213. https://doi.org/10.1029/2010JA015959.

Ip, W.-H., Kimura, H., Liu, C.-P., 1985. Interaction of the cometary dust with the solar wind and cometary plasma. In: Giese, R.H., Lamy, P. (Eds.), IAU Colloq. 85: Properties and Interactions of Interplanetary Dust. Astrophysics and Space Science Library 119. pp. 325–328. https://doi.org/10.1007/978-94-009-5464-9_64.

Jones, G.H., Knight, M.M., Battams, K., Boice, D.C., Brown, J., Giordano, S., Raymond, J., Snodgrass, C., Steckloff, J.K., Weissman, P., Fitzsimmons, A., Lisse, C., Opitom, C., Birkett, K.S., Bzowski, M., Decock, A., Mann, I., Ramanjooloo, Y., McCauley, P., 2018. The science of Sungrazers, Sunskirters, and other Near-Sun Comets. Space Sci. Rev. 214 (1), 20. https://doi.org/10.1007/s11214-017-0446-5.

Karim, A.I.A., 1966. Stability of the fourth order Runge–Kutta method for the solution of systems of differential equations. Comput. J. 9 (3), 308–311.

Kelley, M.S., Woodward, C.E., Harker, D.E., Wooden, D.H., Reach, W.T., Fernández, Y.R., 2010. Comet dust diversity in ground-based and Spitzer Space Telescope Mid-Infrared Spectra. Lunar and Planetary Science Conference. Lunar and Planetary Inst. 41. pp. 2375. Technical Report

Kharchuk, S.V., Korsun, P.P., 2010. Striated features in the dust tail of comet C/2006 P1 (McNaught). Kinematics Phys. Celestial Bodies 26, 322–325. https://doi.org/10.3103/S0884591310060048.

Kimura, H., Liu, C.-P., Jockers, K., 1985. On the dynamic behavior of dust striae observed in comets West 1976 VI, and Mrkos 1957 V. In: Giese, R.H., Lamy, P. (Eds.), IAU Colloq. 85: Properties and Interactions of Interplanetary Dust. Astrophysics and Space Science Library 119. pp. 283–286. https://doi.org/10.1007/978-94-009-5464-9_59.

Koutchmy, S., Lamy, P., 1978. Propagating inhomogeneities in the dust tail of comet west 1975. Nature 273 (5663), 522–524. https://doi.org/10.1038/273522a0.

Kramer, E.A., Fernandez, Y.R., Lisse, C.M., Kelley, M.S., Woodney, L.M., 2014. A

dynamical analysis of the dust tail of comet C/1995 O1 (Hale–Bopp) at high heliocentric distances. Icarus 236, 136–145. https://doi.org/10.1016/j.icarus.2014.03.033.
Kronk, G., 1999. Cometography: Volume 1, Ancient-1799: A Catalog of Comets. Cometography Series. Cambridge University Press. URL: https://books.google.co.uk/books?id=Umxbb68tmZMC
Lamy, P.L., Koutchmy, S., 1979. Comet West 1975n. II - Study of the striated tail. Astron. Astrophys. 72, 50–54.
Lang, D., Hogg, D.W., Mierle, K., Blanton, M., Roweis, S., 2010. Astrometry. net: blind astrometric calibration of arbitrary astronomical images. Astron. J. 139 (5), 1782.
Leblanc, F., Fulle, M., López Ariste, A., Cremonese, G., Doressoundiram, A., Sainz Dalda, A., Gelly, B., 2008. Comet McNaught C/2006 P1: observation of the sodium emission by the solar telescope THEMIS. Astron. Astrophys. 482, 293–298. https://doi.org/10.1051/0004-6361:20078795.
Linker, J.A., Mikić, Z., Biesecker, D.A., Forsyth, R.J., Gibson, S.E., Lazarus, A.J., Lecinski, A., Riley, P., Szabo, A., Thompson, B.J., 1999. Magnetohydrodynamic modeling of the solar corona during Whole Sun Month. J. Geophys. Res. 104, 9809–9830. https://doi.org/10.1029/1998JA900159.
Luhmann, J.G., Solomon, S.C., Linker, J.A., Lyon, J.G., Mikic, Z., Odstrcil, D., Wang, W., Wiltberger, M., 2004. Coupled model simulation of a Sun-to-Earth space weather event. J. Atmos. Sol. Terr. Phys. 66, 1243–1256. https://doi.org/10.1016/j.jastp.2004.04.005.
Marsden, B.G., 2007. Comet C/2006 P1 (McNaught). 8801 IAU Circular.
Marsden, B.G., 2007. Comet C/2006 P1 (McNaught). 8796 International Astronomical Union Circulars.
McClure, A., 1962. Latest Pictures of Comet Seki-Lines. 23 Sky & Telescope.
McNaught, R., 2006. Comet C/2006 P1. 8737. International Astronomical Union Circular, pp. 1.
Mendis, D., Horányi, M., 2013. Dusty plasma effects in comets: expectations for Rosetta. Rev. Geophys. 51 (1), 53–75. https://doi.org/10.1002/rog.20005.
Mikić, Z., Linker, J.A., Schnack, D.D., Lionello, R., Tarditi, A., 1999. Magnetohydrodynamic modeling of the global solar corona. Phys. Plasmas 6, 2217–2224. https://doi.org/10.1063/1.873474.
Minato, T., Köhler, M., Kimura, H., Mann, I., Yamamoto, T., 2004. Momentum transfer to interplanetary dust from the solar wind. Astron. Astrophys. 424 (2), L13–L16. https://doi.org/10.1051/0004-6361:200400037.
Morgan, H., Druckmüller, M., 2014. Multi-scale gaussian normalization for solar image processing. Solar Phys. 289 (8), 2945–2955. https://doi.org/10.1007/s11207-014-0523-9.
Morrill, J.S., Korendyke, C.M., Brueckner, G.E., Giovane, F., Howard, R.A., Koomen, M., Moses, D., Plunkett, S.P., Vourlidas, A., Esfandiari, E., Rich, N., Wang, D., Thernisien, A.F., Lamy, P., Llebaria, A., Biesecker, D., Michels, D., Gong, Q., Andrews, M., 2006. Calibration of the SOHO/LASCO C3 white light coronagraph. Solar Phys. 233 (2), 331–372. https://doi.org/10.1007/s11207-006-2058-1.
Nishioka, K., 1998. Finite lifetime fragment model 2 for synchronic band formation in dust tails of comets. Icarus 134 (1), 24–34.
Nishioka, K., Saito, K., Watanabe, J.-I., Ozeki, T., 1992. Photographic Observations of the Synchronic Band in the Tail of Comet West 1976 VI. 2. Publications of the National Astronomical Observatory of Japan, pp. 601–621.
Nishioka, K., Watanabe, J.-I., 1990. Finite lifetime fragment model for synchronic band formation in dust tails of comets. Icarus 87 (2), 403–411.
Notni, P., Thaenert, W., 1988. The striae in the dust tails of great comets - A comparison to various theories. Astron. Nachr. 309, 133–146. https://doi.org/10.1002/asna.2113090210.
Odstrcil, D., 2003. Modeling 3-D solar wind structure. Adv. Space Res. 32, 497–506. https://doi.org/10.1016/S0273-1177(03)00332-6.
Odstrcil, D., Pizzo, V.J., Linker, J.A., Riley, P., Lionello, R., Mikic, Z., 2004. Initial coupling of coronal and heliospheric numerical magnetohydrodynamic codes. J. Atmos. Sol. Terr. Phys. 66 (15–16), 1311–1320. https://doi.org/10.1016/j.jastp.2004.04.007.
Pittichová, J., Sekanina, Z., Birkle, K., Boehnhardt, H., Engels, D., Keller, P., 1997. An early investigation of the striated tail of comet Hale-Bopp (C/1995 O1). Earth Moon Planets 78 (1/3), 329–338. https://doi.org/10.1023/A:1006242209416.
Schulz, R., Hilchenbach, M., Langevin, Y., Kissel, J., Silen, J., Briois, C., Engrand, C., Hornung, K., Baklouti, D., Bardyn, A., Cottin, H., Fischer, H., Fray, N., Godard, M., Lehto, H., Roy, L.L., Merouane, S., Orthous-Daunay, F.-R., Paquette, J., Rynö, J., Siljeström, S., Stenzel, O., Thirkell, L., Varmuza, K., Zaprudin, B., 2015. Comet 67P/Churyumov-Gerasimenko sheds dust coat accumulated over the past four years. Nature 518 (7538), 216–218. https://doi.org/10.1038/nature14159.
Sekanina, Z., Farrell, J., 1980. The striated dust tail of comet West 1976 VI as a particle fragmentation phenomenon. Astron. J. 85, 1538–1554.
SekaninaZ, Farrell, J.A., 1982. Two dust populations of particle fragments in the striated tail of comet Mrkos 1957 V. Astron. J. 87 (12), 1836. https://doi.org/10.1017/CBO9781107415324.004.
Sekenina, Z., Pittichová, J., 1997. Distribution law for particle fragmentation times in a theory for striated tails of dust comets: application to comet Hale-Bopp (C/1995 O1. Earth Moon Planets 78 (1–3), 339–346.
Steckloff, J.K., Jacobson, S.A., 2016. The formation of striae within cometary dust tails by a sublimation-driven YORP-like effect. Icarus 264, 160–171.
Strub, P., Krüger, H., Sterken, V.J., 2015. Sixteen years of Ulysses interstellar dust measurements in the solar system. II. Fluctuations in the dust flow from the data. Astrophys. J. 812, 140. https://doi.org/10.1088/0004-637X/812/2/140.
Tappin, S.J., Eyles, C.J., Davies, J.A., 2015. Determination of the photometric calibration and large-scale flatfield of the STEREO heliospheric imagers: II. HI-2. Solar Phys. 290 (7), 2143–2170. https://doi.org/10.1007/s11207-015-0737-5.
Wooden, D., De Buizer, J., Kelley, M., Sitko, M., Woodward, C., Harker, D., Reach, W., Russell, R., Kim, D., Yanamadra-Fisher, P., Lisse, C., de Pater, I., Gehrz, R., Kolokolova, L., 2014. Comet C/2012 S1 (ISON)'s carbon-rich and micron-size-dominated coma dust. In: Muinonen, K., Penttilä, A., Granvik, M., Virkki, A., Fedorets, G., Wilkman, O., Kohout, T. (Eds.), Asteroids, Comets, Meteors 2014.